Breakdown mechanisms and heat transfer overshoot in hypersonic zero pressure gradient boundary layers

Kenneth J. Franko† and Sanjiva K. Lele

Department of Aeronautics and Astronautics, Stanford University, Stanford, CA 94305, USA

A laminar Mach 6 flat plate boundary layer is perturbed using three different types of disturbances introduced through blowing and suction. The linear and nonlinear development and eventual breakdown to turbulence are investigated using direct numerical simulation. The three different transition mechanisms compared are first mode oblique breakdown, second mode oblique breakdown and second mode fundamental resonance. The focus of the present work is to compare the nonlinear development and breakdown to turbulence for the different transition mechanisms and explain the heat transfer overshoot observed in experiments. First mode oblique breakdown leads to the shortest transition length and a clear peak in wall heat transfer in the transitional region. For all three transition mechanisms, the development of streamwise streaks precedes the breakdown to fully turbulent flow. The modal linear and nonlinear development are analysed including the breakdown of the streaks. The effect of wall cooling is investigated for second mode fundamental resonance and no qualitative differences in the nonlinear processes are observed. Finally, the development towards fully turbulent flow including mean flow, turbulent spectra, and turbulent fluctuations is shown and the first mode oblique breakdown simulation shows the furthest development towards a fully turbulent flow.

---

1. Introduction

The physical mechanism of boundary layer laminar to turbulent transition for high-speed flows is poorly understood. Transition to turbulence for high Mach number flows is fundamentally different from that of subsonic and supersonic flows. Under hypersonic flow conditions, higher instability modes of an acoustic nature exist, as discovered by Mack (1969). Because of these additional modes and their higher growth rates at high Mach numbers, alternative mechanisms have been suggested as the cause of transition to a fully turbulent flow in high-speed boundary layer flows. The mechanisms for instability growth and breakdown must be understood to predict the transition location. Prediction of transition to turbulence is usually based on the linear growth of the disturbances without considering the nonlinear and breakdown

† Present address: Sandia National Laboratories, Albuquerque, NM 87185, USA. Email address for correspondence: kjfrank@sandia.gov

regimes which precede a fully turbulent flow. In addition, skin friction and heat transfer values have been observed to first overshoot turbulent values in the nonlinear breakdown regime before ultimately relaxing towards turbulent boundary layer values. This overshoot could lead to a localized region of high heat transfer. This work explores different controlled transition scenarios to determine potential mechanisms for breakdown and to compare the nonlinear processes involved for each of these scenarios. In addition, the different transition scenarios are explored to determine how the heat transfer overshoot observed in experiments could be produced.

The determination of the transition mechanism in shock tunnel and wind tunnel measurements is difficult because of the high noise levels (Schneider 2001). The development of turbulent boundary layers on the walls of wind and shock tunnels and fluctuations in the free stream flow introduce disturbances at higher amplitudes than encountered in flight. Quiet tunnels relieve some of these problems, but fully turbulent flow at hypersonic flow conditions is difficult to obtain because of the limitations of Reynolds number of these facilities. Second mode instabilities are considered to be the dominant instabilities for high Mach number flows. Detailed work comparing linear second mode growth compared with linear stability theory has been undertaken in both quiet (Wilkinson 1997; Alba *et al.* 2010) and noisy tunnels (Stetson & Kimmel 1992). However, the breakdown mechanism has not yet been clearly determined.

While second mode instabilities are often stated to be dominant for flows above Mach 5, only the growth rates for second mode instabilities are largest. The N factors for first mode instabilities may be larger than those of second mode instabilities even for high Mach numbers, depending on the geometry and thermal boundary conditions. For example, on an adiabatic flat plate, Masad (1993) computed a cross-over from first mode to second mode dominance based on the e^N method at a Mach number of 6.5. For the case of a blunted geometry, the edge Mach number could be much lower than the free stream Mach number. The e^N method does not take into consideration nonlinear effects which may be different for first and second mode instabilities. In addition, the fluctuations in noisy tunnels at lower frequencies typical of first mode instabilities have higher amplitudes than the frequencies typical of second mode instabilities (Schneider 2001). Both first and second mode instabilities may be excited through free stream sound (Ma & Zhong 2005). Detailed recent experimental, theoretical and computational studies of high-speed receptivity can be found in the work of Maslov *et al.* (2001), Fedorov (2003) and Ma & Zhong (2003*a*,*b*, 2005). In conclusion, first mode instabilities still need to be considered in addition to second mode instabilities for flows with free stream Mach numbers above 5.

Direct numerical simulation (DNS) has been used as a tool to illuminate potential transition scenarios. Usually these simulations approach the problem in one of two ways. The first employs broadband forcing of multiple frequencies and deliberate excitation of many instability waves. Wave packet simulations and turbulent spot simulations such as those by Krishnan & Sandham (2006) and Sivasubramanian & Fasel (2010) take this approach. The initial computations undertaken for the present work by Franko, Bhaskaran & Lele (2011) used large-amplitude forcing using narrow square wave periodic function in time and a Gaussian in space. A significant overshoot in heat transfer was observed in the transitional region. It is very difficult to analyse the nonlinear behaviour and eventual breakdown mechanism from such data because multiple modes and transition scenarios may be occurring simultaneously. The approach undertaken in the present work is to selectively force one or two dominant instability waves at set frequencies and spanwise wavenumbers to investigate specific transition scenarios. This second method is not representative of flight or wind tunnels

where there is a large spectrum of instabilities that could be excited, but it can be used to elucidate the specific transition mechanism and in particular is useful in explaining potential mechanisms for heat transfer overshoot. In a realistic flow, these different mechanisms are occurring at the same time, competing and potentially interacting.

DNS studies using the second approach have been used to investigate a variety of potential transition mechanisms. The subharmonic and fundamental resonance mechanisms begin with the growth of a two-dimensional instability wave. In the case of high-speed flows, the two-dimensional wave is typically a Mack second mode instability, because they have the largest growth rates. Once the two-dimensional wave grows large enough, a secondary oblique instability begins to grow at either the same frequency (fundamental resonance) or a subharmonic frequency (subharmonic resonance). Adams & Kleiser (1996) investigated subharmonic resonance mechanism in the temporal context with a constant base flow enforced. The secondary instability of the subharmonic oblique mode was strong and the flow began to break down to turbulence. However, because a constant base flow was enforced, the growth rate of the two-dimensional Mack mode was constant and the flow was not representative of a spatially developing boundary layer. Another DNS study (Husmeier & Fasel 2007) has shown that the subharmonic resonance is weaker than the fundamental resonance in the spatial context. The latter, however, has been suggested as a possible breakdown mechanism (Kloker 2002; Koevary *et al.* 2010), but has not been shown to lead to fully turbulent flow. Oblique breakdown for first mode instabilities in supersonic flows has been shown to lead to a fully turbulent flow (Mayer, von Terzi & Fasel 2011). Pruett & Chang (1995) studied the possibility of transition caused by oblique second mode instabilities as the primary instabilities. The computation was run until the strongly nonlinear stage, but because of computational costs did not include full breakdown or a completely turbulent flow due to the large extent of the transitional region.

Other DNS studies have been undertaken for turbulent boundary layer flows. For the Mach number under study herein, the temporal DNS computations in the work of Martin (2007) and Duan, Beekman & Martin (2010, 2011) are most relevant. They studied the effects of wall temperature and Mach number on turbulent mean and statistical quantities. Table 1 gives a brief summary of the Mach number, Reynolds number and resolution in wall units of some recent DNS computations of supersonic and hypersonic transitional and turbulent boundary layer flows. The grid resolution of the current study is comparable, particularly with the one simulation of Duan *et al.* (2011) that has a Mach number and wall temperature similar to the present study. Comparison of the results of this work will be made with some of these previous studies

The overshoot of skin friction and heat transfer in the transitional region over the expected values for the turbulent region has been observed in numerous experiments and only a sample will be mentioned here. For hypersonic flows, heat transfer is the quantity of greatest importance and usually easier to determine experimentally. Experiments for both cones and flat plates have observed overshoots in heat transfer. For hypersonic flat plate boundary layers investigated at CUBRC (Holden 1972), clear overshoots of the heat transfer in the transitional region are observed for the majority, but not all, of the flow conditions investigated. Most recently, measurements taken in the CUBRC wind tunnel on HIFiRE-1 vehicle models (Wadhams *et al.* 2008) produced heat transfer curves with overshoots past the turbulent correlation values for some experimental conditions (see figure 1). The overshoots occurred when transition occurred earlier for the model, for the case with smaller nose bluntness.
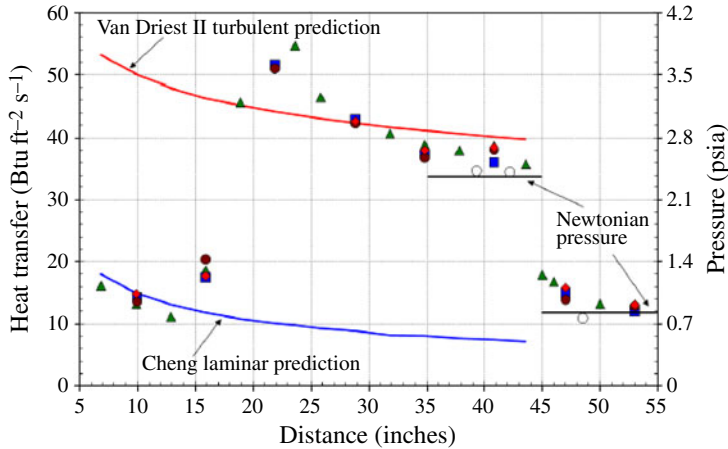
FIGURE 1. (Colour online) Experimental wall heat transfer and pressure on HIFiRE-1 forebody at Mach 6.5 with a 2.5 mm diameter nose tip, with semi-empirical prediction. The different solid symbols represent heat transfer measurements at four different axial rays. The open circles are pressure measurements at the surface. Reproduced from Wadhams *et al.* (2008).

Studies	Duan (1)	Pirozzoli (2)	Mayer (3)	Guarini (4)	Present study
Mach	5.81	2.25	3	2.5	6
Δx^+_{max}	7.8	14.50	3.32	8.86	4.43
$\Delta y^+_{wall,max}$	0.30	1.05	0.49	0.48	0.32
Δz^+_{max}	3.1	6.56	1.35	5.91	2.97
$Re_{\theta,max}$	5775.1	4250	1985	1600	2652
Temporal or spatial	temporal	spatial	spatial	temporal	spatial

TABLE 1. Summary of DNS computations of transition and turbulence in supersonic and hypersonic boundary layers. Present study is for first mode oblique breakdown case. References: (1) Duan *et al.* (2011), (2) Pirozzoli *et al.* (2004), (3) Mayer *et al.* (2011), (4) Guarini *et al.* (2000).

When the bluntness was increased, the transition location moved downstream and no overshoot was observed. Similar results were presented for straight cones and flared cones at Mach 6 in the NASA Langley experiment by Horvath, Berry & Hollis (2002). Heat transfer overshoot was also observed to decrease with increasing nose bluntness. Nose bluntness stabilizes both first and second mode disturbances according to linear stability theory, due to effects of the entropy layer (Malik, Spall & Chang 1990), however, the physical mechanism responsible for overshoot is currently unknown.

An overshoot in skin friction has also been observed in recent DNS studies of transitional and turbulent boundary layers with different forcing and flow conditions. The breakdown of streamwise streaks in incompressible flow shows a clear overshoot in the skin friction (Brandt & Henningson 2002; Schlatter *et al.* 2008). The increase in skin friction is attributed to the nature of the secondary instability of the streamwise streaks. The secondary instability of the streaks leads to the generation of quasi-

streamwise vorticity, which then increases the wall shear stress. Mayer *et al.* (2011) computed in detail the transition of a Mach 3.0 boundary layer due to oblique breakdown. The interaction of the oblique waves leads to the generation of streamwise vortices, which may be responsible for the observed overshoot in computed skin friction. Pirozzoli, Grasso & Gatski (2004) used a single frequency and multiple spanwise wavenumber forcing to produce a turbulent boundary layer. The focus of the work was not transition, but the resulting skin friction curve also contains a significant overshoot that later collapses well on top of the turbulent correlation.

Potential transition mechanisms are suggested by previous computational work and experiments where heat transfer overshoot is observed. Three different transition scenarios are explored in this paper to analyse mechanisms for breakdown to turbulence and the observed overshoot in wall heat transfer. The first mechanism is first mode oblique breakdown, which has been shown to lead to transition for a variety of supersonic flows (Thumm, Wolz & Fasel 1989; Jiang *et al.* 2006; Mayer *et al.* 2011) along with overshoots in skin friction. In this work, it is shown to produce the shortest transitional region and an overshoot past turbulent correlation values for both skin friction and heat transfer. It will be referred to as the 'first mode oblique breakdown' case, sometimes abbreviated to first OB. Two other possible mechanisms involve higher-frequency Mack second mode instabilities. For the second case, a two-dimensional Mack second mode is forced to investigate the possibility of either subharmonic or fundamental resonance. After exploration it was determined that the fundamental resonance was much stronger than subharmonic resonance and therefore this case will be referred to as the 'second mode fundamental resonance' case, sometimes abbreviated second FR. For the third case, two oblique Mack second mode waves are forced at the same frequency as the second mode fundamental resonance case, but with a non-zero spanwise wavenumber. The forcing is very similar to the first mode oblique breakdown, except that a higher-frequency Mack second mode is forced. It will be referred to as the 'second mode oblique breakdown' case, sometimes abbreviated as second OB. The transition length in both the second mode fundamental resonance and second mode oblique breakdown forcing cases is significantly longer than the transition length in the first mode oblique breakdown case. For the second mode fundamental resonance case, no overshoot in either skin friction or heat transfer is observed. For the second mode oblique breakdown case, an overshoot in only heat transfer is observed, although it is less pronounced than in the oblique breakdown case. The transition mechanisms are studied in detail including modal decompositions. For all three cases, streaks play an important role in the eventual breakdown, and the generation of streaks and their breakdown are analysed.

2. Simulation details

In the current study, the flat plate boundary layer is used to study different potential transition mechanisms at a free stream Mach number of 6. The flat plate boundary layer is the canonical problem for studying boundary layers and allows for study of the transition process without having to consider the effects of surface curvature or a leading edge shock. The inflow and initial conditions are determined using a compressible similarity solution and the disturbances are introduced through suction and blowing at the wall near the leading edge of the domain. Because the compressible similarity solution is a solution of the boundary layer equations and not the full Navier–Stokes equations, there is a slight adjustment of the mean flow in the flow solver. The inflow conditions for the simulations are chosen to match those of
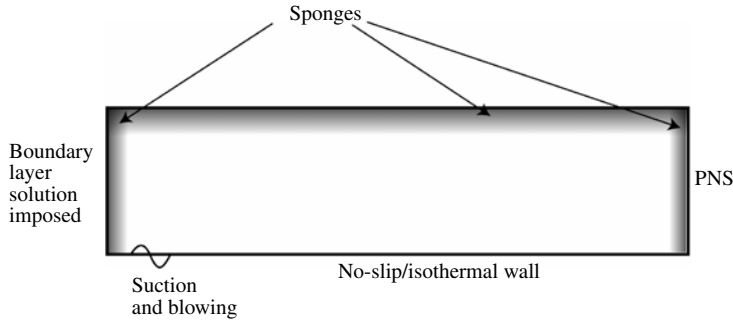
FIGURE 2. Sketch of the DNS domain with boundary conditions.

Case	First mode oblique breakdown	Second mode fundamental resonance	Second mode oblique breakdown
x_{max}	1000	1500	1875
y_{max}	75	50	50
z_{max}	62.83	50.27	62.83
nx	2048	2432	3040
ny	200	150	150
nz	192	64	96
Δx_{max}^{+}	4.43	4.99	5.08
$\Delta y_{wall,max}^{+}$	0.32	0.25	0.43
Δz_{max}^{+}	2.97	6.35	5.39
Forcing amplitude	$0.05U_e$	$0.1U_e$	$0.05U_e$
$Re_{\theta,max}$	2652	2268	1985
T_w/T_e	6.5	6.5	6.5
Forcing periods averaged for results	6	15	12

TABLE 2. Summary of DNS computations of transition.

the turbulent spot simulation of Krishnan & Sandham (2006) because their simulation leads to the generation of a turbulent spot. For all cases, the Reynolds number (Re) based on inflow displacement thickness and free stream density, viscosity, and velocity is 3000 and $x = 0$ at the inflow. All lengths are non-dimensionalized by the inlet displacement thickness (δ_{in}^*). Figure 2 shows a sketch of the domain along with the boundary conditions. The domain is rectangular with even spacing in the spanwise and streamwise directions and with grid stretching in the direction normal to the wall. An isothermal wall at a temperature ($T_w/T_e = 6.5$) close to the laminar adiabatic wall temperature is used. A summary of the domain size, number of grid points and resolution for the three different transition scenarios can be found in table 2.

2.1. Numerical method

The general curvilinear form of the compressible Navier–Stokes equations is solved in non-dimensional conservation form as

$$\frac{\partial \rho}{\partial t} + \frac{\partial (\rho u_i)}{\partial x_i} = 0, \tag{2.1}$$

$$\frac{\partial(\rho u_i)}{\partial t} + \frac{\partial(\rho u_i u_j + g^{ij}p - \tau_{ij})}{\partial x_j} = 0, \tag{2.2}$$

$$\frac{\partial E}{\partial t} + \frac{\partial\left[(E+p)u_j - \tau_{ij}g_{ik}u_k + q_j\right]}{\partial x_j} = 0, \tag{2.3}$$

where u_i, ρ and p are the contra-variant velocity components, density and pressure, respectively. The total energy, E, the viscous stress tensor, τ_{ij}, and the heat flux for a fluid obeying Fourier's law, q_j, are given by

$$E = \frac{p}{\gamma - 1} + \frac{1}{2}\rho g_{ij}u_i u_j, \tag{2.4}$$

$$\tau_{ij} = \frac{\mu}{Re_a}\left(g^{jk}\frac{\partial u_i}{\partial x_k} + g^{ik}\frac{\partial u_j}{\partial x_k}\right) + \left[\tilde{\beta} - \frac{2}{3}\frac{\mu}{Re_a}\right]g^{ij}\frac{\partial u_k}{\partial x_k}, \tag{2.5}$$

and

$$q_j = -\left[\frac{\kappa}{Re_a Pr} + \tilde{\kappa}\right]g^{ij}\frac{\partial T}{\partial x_i}. \tag{2.6}$$

Assuming the medium to be a calorically perfect gas, the set of equations is closed by the equation of state

$$p = \frac{\gamma - 1}{\gamma}\rho T. \tag{2.7}$$

In the equations above, g_{ij} and g^{ij} are the covariant and contra-variant metric tensors, respectively. Dimensional variables are starred throughout this paper. The equations are solved in non-dimensional form, where length, velocity components, density, pressure and temperature are non-dimensionalized by the inlet displacement thickness, δ_{in}^*, speed of sound, c_∞^*, free stream density, ρ_∞^*, pressure scale, $\gamma\rho_\infty^* c_\infty^{*2}$, and temperature scale, $(\gamma - 1)T_\infty^*$, respectively. T^* is the temperature, γ is the ratio of specific heats, Re_a is the Reynolds number based on the free stream speed of sound defined as $Re_a = \rho_\infty^* c_\infty^* \delta_{in}^*/\mu_\infty$ and Pr is the Prandtl number defined as $Pr = \mu_\infty^* C_p^*/\kappa_\infty^*$. Results are presented using the Reynolds number based on the free stream velocity $Re = \rho_\infty^* U_\infty^* \delta_{in}^*/\mu_\infty = M_\infty Re_a$. Here, C_p^* is the heat capacity at constant pressure, μ^* is the viscosity and κ^* is the thermal conductivity. $\tilde{\beta}$ and $\tilde{\kappa}$ are the artificial bulk viscosity and thermal conductivity which are used for shock capturing and are described in §2.3. The Einstein notation is used in the equations and, therefore, repeated indices are summed over.

The numerical scheme for spatial discretization is a sixth-order accurate compact scheme implemented on a staggered grid; see Nagarajan, Lele & Ferziger (2003) for details. Compact finite-difference schemes are non-dissipative and numerical instabilities arising from insufficient grid resolution, mesh non-uniformities, approximate boundary conditions and interpolation at grid interfaces have to be filtered to preserve stability of the numerical schemes. The high wavenumber compact filter presented by Lele (1992) is applied to the computed solution at prescribed time intervals in order to control numerical instabilities. The time integration of the fluid equations is carried out by a fully implicit second-order Beam–Warming scheme (Beam & Warming 1978) in order to overcome the time step restriction. The second-

order implicit method is given by

$$\frac{3Q^{n+1} - 4Q^n + Q^{n-1}}{2\Delta t} = f(Q^{n+1}, t^{n+1}). \tag{2.8}$$

The right-hand side is solved through approximate factorization followed by diagonalization of the implicit matrix in the x and z directions. Details of the approximate factorization are presented by Nagarajan (2004).

2.2. *Boundary conditions*

Inflow, outflow, free stream and wall boundary conditions are needed at the four edges of the rectangular domain. The domain is periodic in the spanwise direction. Supersonic inflow boundary conditions are used. All of the flow variables are set at the inflow based on a compressible boundary layer similarity solution. For the outflow, a boundary condition based on the parabolized Navier–Stokes (PNS) equations is used (Collis 1997). The PNS equations are derived from the full governing equations by removing the streamwise elliptic (viscous) and the upstream propagating hyperbolic (acoustic wave) terms. When using the PNS equations, the pressure gradient is incorrectly predicted and instead an *a priori* estimate of the pressure gradient is used and included as a source term. In this work, the estimate for the pressure gradient at the outflow is obtained from the initial laminar boundary layer solution.

Characteristic boundary conditions based on Riemann invariants are applied at the free stream boundary. The boundary is treated as a subsonic outflow boundary. For a subsonic outflow boundary, one incoming quantity must be specified along with four outgoing quantities computed from the interior domain. Here, the incoming Riemann invariant is imposed and the entropy, streamwise and spanwise velocities and outgoing Riemann invariant are computed by extrapolation from the interior nodes neighbouring the outflow boundary.

A damping sponge layer is also applied along the inflow, outflow and free stream boundaries to minimize reflections of disturbances (Nagarajan 2004; Bhaskaran 2010). In the sponge layers, the following relaxation term is added to the governing equations:

$$-\sigma(Q - Q_{ref}), \tag{2.9}$$

where σ is the sponge strength specified as

$$\sigma = \begin{cases} 0 & \text{if } x < x_{sponge}, \\ A\left(\dfrac{x - x_{sponge}}{L - x_{sponge}}\right)^n & \text{if } x \geqslant x_{sponge}. \end{cases} \tag{2.10}$$

Here, x_{sponge} is the starting sponge location and L is the full length of the sponge layer. The sponge effect vanishes at the starting location and gradually grows in strength as the maximum size of the sponge is reached. The sponge reference solution, Q_{ref}, is specified as the initial laminar boundary layer, which is determined by a compressible boundary layer similarity solution. The constants A and n used in the present computations are $A = 20$ and $n = 4$.

2.3. *Shock capturing*

Turbulent high-speed boundary layers spontaneously develop eddy-shocklets which necessitate a shock capturing scheme for the simulations to maintain numerical stability. A common approach for high-order methods based on compact finite

differences is the addition of artificial viscosity and thermal conductivity only in regions containing shocks (Cook & Cabot 2004, 2005). The current implementation is based on the formulation of Kawai, Shankar & Lele (2010) called LAD (localized artificial diffusivity). The specific implementation used is the method LAD-D2-0 in Kawai *et al.* (2010). The advantage of compact finite difference schemes with localized artificial diffusivity over other high-order methods such as WENO for compressible turbulence simulations is demonstrated by Johnsen *et al.* (2010). The WENO scheme in particular is shown to be excessively dissipative for a compressible isotropic turbulence simulation.

Artificial bulk viscosity (β^*) and thermal conductivity (κ^*) are added to the physical transport properties in (2.5) and (2.6). The artificial fluid properties are given by

$$\tilde{\beta} = C_\beta \rho f_{sw} \overline{\left| \sum_{l=1}^{3} \frac{\partial^4 \boldsymbol{\nabla} \cdot \boldsymbol{u}}{\partial \xi_l^4} \Delta \xi_l^4 \Delta_{l,\beta}^2 \right|}, \tag{2.11}$$

$$\tilde{\kappa} = C_\kappa \frac{\rho c}{T} \overline{\left| \sum_{l=1}^{3} \frac{\partial^4 e}{\partial \xi_l^4} \Delta \xi_l^4 \Delta_{l,\kappa} \right|}, \tag{2.12}$$

where C_β and C_κ are constant coefficients with values of 1.0 and 0.1 and f_{sw} is a switching function to turn off artificial bulk viscosity in regions of fluid expansion:

$$f_{sw} = H(-\boldsymbol{\nabla} \cdot \boldsymbol{u}) \frac{(\boldsymbol{\nabla} \cdot \boldsymbol{u})^2}{(\boldsymbol{\nabla} \cdot \boldsymbol{u})^2 + |\boldsymbol{\nabla} \times \boldsymbol{u}|^2 + \epsilon}, \tag{2.13}$$

where H is the Heaviside function and ϵ is a small positive constant of value 10^{-14} in order to avoid division by zero. The overline denotes a Gaussian filtering procedure. $\Delta_{l,\beta}$ and $\Delta_{l,\kappa}$ are the local physical grid spacing at the location of the shock. $\Delta \xi_l$ is the grid spacing in computational space and is set to 1. More details of the shock capturing scheme are found in Kawai *et al.* (2010).

2.4. *Disturbance forcing*

The focus of this work is on controlled transition scenarios with specifically chosen instability wave frequencies and spanwise wavenumbers rather than the broadband forcing of Krishnan & Sandham (2006) or the impulse forcing case in Franko *et al.* (2011). In Franko *et al.* (2011) impulsive forcing did produce an overshoot in heat transfer, but it was determined that the transition process was similar to first mode oblique breakdown except with multiple frequencies and spanwise numbers excited. In this work, the disturbance frequencies and spanwise wavenumbers are chosen based on linear stability theory. To study the nonlinear portion of the flow at reduced computational cost, the initial forcing is strong to avoid computing a long linear region. Computations with lower initial forcing were also undertaken and modal development is compared for the first mode oblique breakdown case to show that the modes generated and the overshoot mechanism are not affected by large initial forcing. Suction and blowing at the wall are used to excite the instability waves in the boundary layer. This is a common method to excite disturbances for the purpose of studying boundary layer transition in both computations and experiments. The suction and blowing is of the form

$$v_{wall} = f(x)g(z) \sum_{i}^{\# \, of \, modes} A_i \sin(\omega_i t - \beta_i z) \tag{2.14}$$
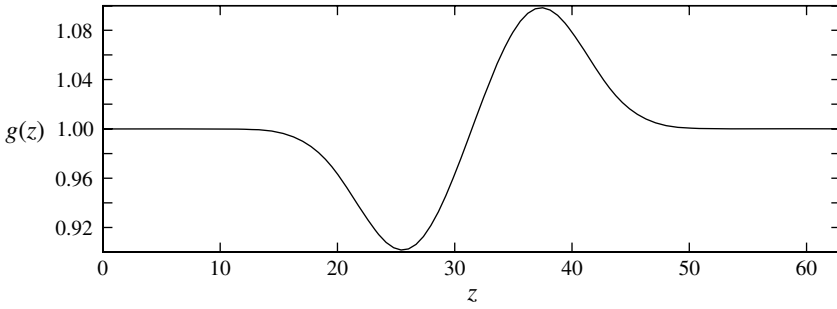
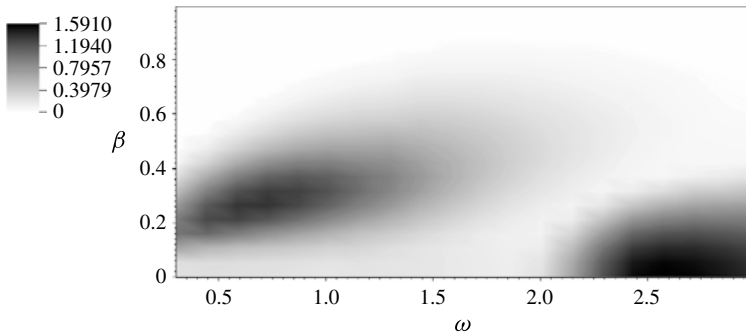FIGURE 3. $g(z)$ function for first mode oblique breakdown case.

FIGURE 4. N factors as a function of non-dimensionalized disturbance frequency, $(\omega = \omega^* \delta^*_{in}/c^*_\infty)$ and spanwise wavenumber $(\beta = \beta^* \delta^*_{in})$ for a $M = 6.0$ flat plate boundary layer from a similarity boundary layer solution. N factors integrated from $x = 0$ until $x = 500$.

where the $f(x)$ and $g(z)$ define the variation of the suction and blowing in the x and z directions. The suction and blowing in the x-direction is over a strip with a strength that varies as a Gaussian:

$$f(x) = e^{-(x-x_0)^2/2\sigma^2}. \tag{2.15}$$

In the z-direction, additional variation is added in order to break symmetry. The function is based on the function used by Wang, Lele & Moin (1996) in their incompressible DNS study:

$$g(z) = 1.0 + 0.1(e^{-[(z-z_c-z_w)/z_w]^2} - e^{-[(z-z_c+z_w)/z_w]^2}), \tag{2.16}$$

where z_w is chosen based on the domain width and z_c is the centre of the spanwise domain. Figure 3 shows this function for the first mode oblique breakdown case. The choice for forcing frequency and spanwise wavenumber is determined based on linear stability theory. Figure 4 shows the N factors computed using the boundary layer similarity solution as the base flow. The N factors are determined by integrating the growth factors from $x = 0$ until $x = 500$. Although these N factors are low in comparison to the threshold for typical e^N methods, the high forcing amplitudes used in these simulations allow for shorter linear regimes.

The forcing for each of the cases is different. Frequency is non-dimensionalized by inlet displacement thickness and speed of sound, $\omega = \omega^* \delta^*_{in}/c^*_\infty$, and wavenumber
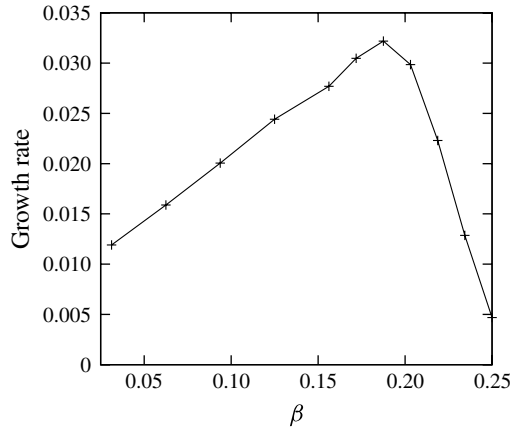
FIGURE 5. Growth rate of secondary instability as a function of spanwise wavenumber for fundamental resonance.

is non-dimensionalized by inlet displacement thickness, $\beta = \beta^* \delta_{in}^*$. Alternatively, a commonly used frequency measure, $F = 2\pi \mu_\infty^* f^* / (\rho_\infty^* U_\infty^{*2})$, can be computed from ω as $F = \omega / (M_\infty Re)$ and is also reported. For all cases, in the streamwise direction the suction and/or blowing is applied between $15 < x < 20$ in the shape of a Gaussian. For the first mode oblique breakdown case, two oppositely oriented oblique first mode instability waves are forced using suction and blowing with a frequency of $\omega = 0.9$ ($F = 5 \times 10^{-5}$) and a spanwise wavenumber of $\beta = 0.3$, each with an amplitude of $v_{wall} = 0.05 U_e$. For the second mode fundamental resonance case, the primary wave is a two-dimensional second mode forced using suction and blowing with a frequency of $\omega = 2.4$ ($F = 1.333 \times 10^{-4}$) and a spanwise wavenumber of $\beta = 0$ with an amplitude of $v_{wall} = 0.1 U_e$, but additional three-dimensional disturbances are added at low amplitudes. Table 3 contains the details of the modes excited for the second mode fundamental resonance case. Additional modes are excited in order to introduce three-dimensionality and to determine whether subharmonic or fundamental resonance is observed. Oblique disturbances are excited at both the same frequency and a subharmonic of the primary two-dimensional instability mode frequency. Because the fundamental resonance mechanism has been shown to be stronger than subharmonic resonance (Husmeier & Fasel 2007), multiple exploratory computations at a coarser resolution than DNS were run to determine which oblique disturbances are experience the strongest fundamental resonance growth. Figure 5 shows the growth rate extracted at $x = 300$ of different oblique disturbances with the same frequency. The secondary growth curve will change depending on the x location chosen for extraction. Disturbances of the same frequency as the fundamental disturbance with spanwise wavenumbers of 0.125 and 0.25 are introduced through suction and blowing. For the second mode oblique breakdown case, two oblique second mode instability waves of opposite orientation with a frequency of $\omega = 2.4$ ($F \approx 1.333 \times 10^{-4}$) and a spanwise wavenumber of $\beta = 0.1$ are forced using suction and blowing with an amplitude of $v_{wall} = 0.05 U_e$.

An alternative classification of instability waves, particularly for receptivity processes, exists based on their behaviour near the leading edge of the plate (Fedorov 2003). Modes are labelled as either S (slow) or F (fast) modes. For modes where the phase speed approaches $1 - 1/(M \cos \theta_z)$ or the phase speed of the slow acoustic mode,

Mode	ω	β	Amplitude (U_e)
1	2.4	0	0.1
2	1.2	0	0.005
3	0.0	0.125	0.005
4	0.0	0.25	0.005
5	1.2	0.125	0.005
6	1.2	−0.125	0.005
7	2.4	0.25	0.005
8	2.4	−0.25	0.005
9	2.4	0.125	0.005
10	2.4	−0.125	0.005

TABLE 3. Modes excited and their amplitudes for the second mode fundamental resonance case.

the modes are labelled as S modes. θ_z is the wave angle ($\tan^{-1}(\beta/\alpha)$). For modes where the phase speed approaches $1 + 1/(M\cos\theta_z)$ or the phase speed of the fast acoustic mode, the modes are labelled as F modes. In these computations, since the flat plate is nearly adiabatic, both the first and second mode instabilities excited are S modes. This is confirmed by tracking the phase speed of each instability mode as $Re \rightarrow 0$. The phase speeds of both first mode and second mode instabilities approach $1 - 1/(M\cos\theta_z)$. This classification is particularly important for receptivity processes where free stream acoustic waves can excite instabilities near the leading edge of the flat plate. Fedorov (2011) contains a detailed review of studies of high-speed receptivity and different potential transition scenarios based on this classification.

3. Results

Results for all three cases are presented with a focus on the transition location and transition zone length, the overshoot in heat transfer and turbulent development. Different measures of transition location including skin friction and wall heat transfer are first presented. The flow field is then decomposed into different modes based on frequency and spanwise wavenumber to determine the transition mechanism and its effect on the heat transfer overshoot. Further analysis of the skin friction and wall heat transfer overshoot is then presented. Finally, turbulent flow quantities including mean flow and fluctuations are presented to demonstrate the development from laminar to transitional to fully turbulent flow.

3.1. *Transition location*

The transition location does not have a unique definition for high speed flows. Different methods of defining transition location are typically used for experiments and do not always agree (Stetson & Kimmel 1993). In this work, three different definitions of transition are explored and compared. The first two criteria are based on wall heat transfer rate, skin friction coefficient and boundary layer thickness measurements. These measurements are accessible in hypersonic experiments. Because simulations are used and not experiments, additional data can easily be extracted. The third transition location criterion is based on the spanwise turbulent spectrum, which is difficult to obtain in hypersonic experiments but is a useful measure of development towards a fully turbulent flow. The three different criteria for boundary layer transition differ in transition location and show the difficulty in uniquely defining a transition location.

The first measures of transition location are skin friction and wall heat transfer. Wall heat transfer, in particular, is a useful measure of transition location for experiments for high-speed flows because it can be measured on the model surface and is easier to determine than skin friction. Non-dimensionalized measures of skin friction and wall heat transfer are used to make comparisons. The transition location definition used for both skin friction and wall heat transfer coefficients is the location where the values reach a minimum. In addition, the skin friction and heat transfer are compared with laminar and turbulent correlations. The skin friction coefficient is defined as

$$C_f = \frac{\tau_w^*}{\frac{1}{2}\rho_e^* U_e^{*2}} = \frac{\tau_w}{\frac{1}{2}\rho_e U_e^2 Re}, \tag{3.1}$$

where starred variables are dimensional. The wall heat transfer is characterized by the Stanton number, which is defined as

$$St = \frac{q_w^*}{\rho_e^* U_e^* C_{pe}^* (T_{aw}^* - T_w^*)} = \frac{q_w}{Re Pr \rho_e U_e (T_{aw} - T_w)}, \tag{3.2}$$

where the adiabatic wall temperature for turbulent flow is estimated using the common approximation for recovery factor of $r = Pr^{1/3}$ (White 2006):

$$T_{aw} = T_e \left(1 + r\frac{\gamma - 1}{2} M_e^2 \right). \tag{3.3}$$

The compressible laminar skin friction coefficient is compared to the correlation for a compressible flat plate boundary layer (White 2006):

$$C_{f,lam} = \frac{0.664\sqrt{\rho_w \mu_w / \rho_e \mu_e}}{\sqrt{Re_x}}. \tag{3.4}$$

The turbulent skin friction is compared to the Van Driest II correlation for turbulent compressible flat plate boundary layers. The Van Driest II correlation has been shown to agree well with a large number of experiments of zero pressure gradient compressible boundary layers (Bradshaw 1977). The skin friction coefficient can be computed by solving a nonlinear equation iteratively for C_f:

$$\frac{\sin^{-1}A + \sin^{-1}B}{\sqrt{C_f(T_{aw}/T_e - 1)}} = 4.15 \log \left(Re_{xv} C_f \frac{\mu_e}{\mu_w} \right) + 1.7, \tag{3.5}$$

where

$$A = \frac{2a^2 - b}{(b^2 + 4a^2)^{1/2}} \quad B = \frac{b}{(b^2 + 4a^2)^{1/2}} \tag{3.6}$$

and

$$a = \left(r\frac{\gamma - 1.0}{2} M_e^2 \frac{T_e}{T_w} \right)^{1/2} \quad b = \left(\frac{T_{aw}}{T_w} - 1 \right). \tag{3.7}$$

The Reynolds number for the Van Driest II correlation (Re_{xv}) is not based on the streamwise distance from the leading edge, but instead is based on a virtual origin. The location of the virtual origin (x_v) is arbitrary, but in this case is taken to be the transition location based on skin friction, i.e. where the skin friction coefficient reaches a minimum. The value of x_v for each of the cases is shown in table 4 in the row $x_{tr,Cf}$.

Case	First mode oblique breakdown	Second mode fundamental resonance	Second mode oblique breakdown
$x_{tr,Cf}$	375.7	816.9	784.8
$x_{tr,St}$	329.8	817.5	784.8
$x_{tr,\theta}$	440.2	857.2	892.8
$x_{tr,\theta H}$	452.0	920.6	911.5
$x_{tr,end}$	678.5	1327	1596
$x_{tr,end} - x_{tr,Cf}$	302.8	510.1	811.2

TABLE 4. Transition locations defined by different criterion and transition zone length.

The Reynolds number used is then

$$Re_{xv} = \frac{\rho_e U_e (x - x_v)}{\mu_e}. \tag{3.8}$$

The Stanton number is then computed from the skin friction coefficient using the Reynolds analogy (White 2006):

$$St = \frac{C_f}{2Pr^{2/3}}. \tag{3.9}$$

Figure 6 shows the skin friction and heat transfer averaged across the span and in time as a function of the streamwise coordinate x for the first mode oblique breakdown case. Close to the inflow boundary, there is a large spike due to the suction and blowing that is present in all the cases. The dot-dashed line denotes the laminar correlation for skin friction coefficient. The skin friction coefficient of the computation matches with the laminar correlation until approximately $x = 400$. The transition location based on skin friction ($x_{tr,Cf}$) and wall heat transfer ($x_{tr,St}$) minimum are 375.7 and 329.8, respectively. The skin friction rapidly departs from the laminar value and quickly approaches and exceeds the value predicted by the turbulent correlation. The overshoot beyond the fully turbulent value persists from $x = 550$ until $x = 850$. After $x = 850$ the skin friction coefficient matches well with the turbulent correlation. The Stanton number follows similar behaviour except that the overshoot region is smaller from only $x = 550$ until $x = 650$ and contains a second peak. Further analysis and discussion of the overshoot behaviour is given in § 3.4.

Figure 7 shows the skin friction coefficient and Stanton number averaged across the span and in time as a function of streamwise distance for the second mode fundamental resonance case. The transition location based on skin friction and wall heat transfer minimum are 816.9 and 817.5, almost the same location. However, the skin friction does not reach the turbulent correlation values before the end of the domain and is still rising when it reaches the numerical sponge and outflow boundary. Even though the skin friction and wall heat transfer depart from the laminar values, the transition zone is much longer than in the first mode oblique breakdown case. The transition mechanism will be discussed further in § 3.4. The Stanton number, however, approaches the turbulent correlation values near the end of the domain. Both the skin friction and wall heat transfer coefficients approach the turbulent values from below and there is no tendency for them to overshoot the turbulent values. The peak in skin friction coefficient and Stanton number near $x = 550$ is caused by the
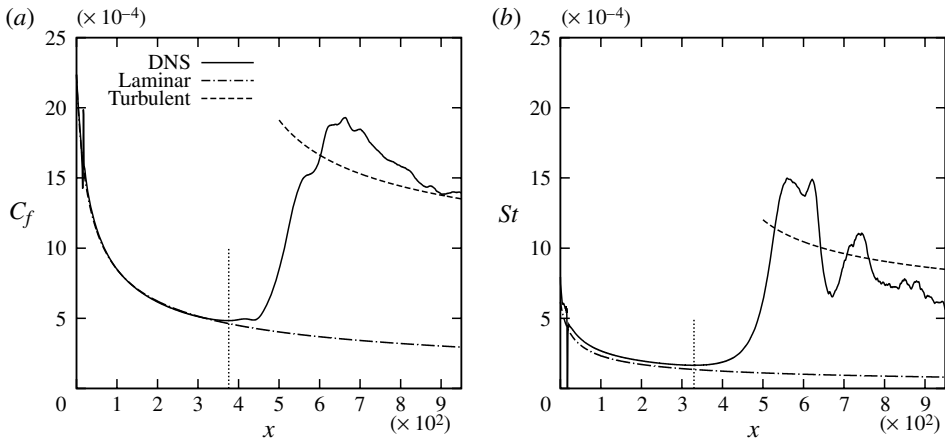
FIGURE 6. Skin friction coefficient and Stanton number averaged in span and time for the first mode oblique breakdown case. Turbulent correlations are computed from semi-empirical Van Driest II correlation and the Reynolds analogy. Dotted vertical lines denote transition locations.
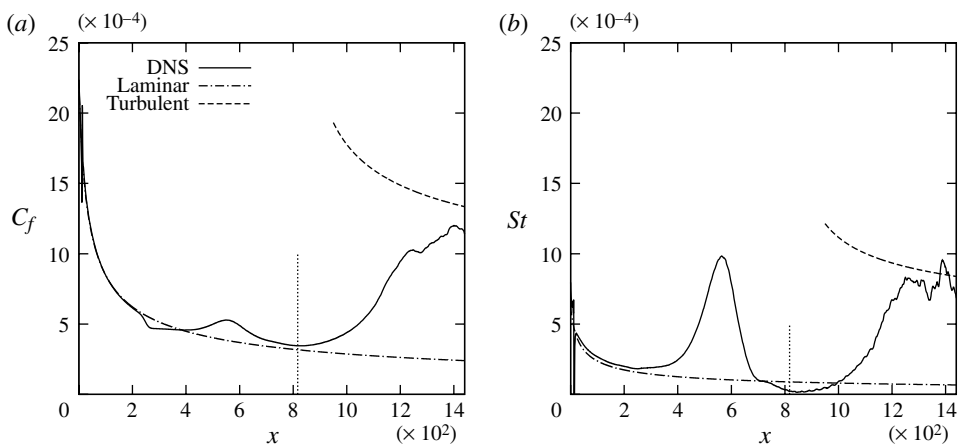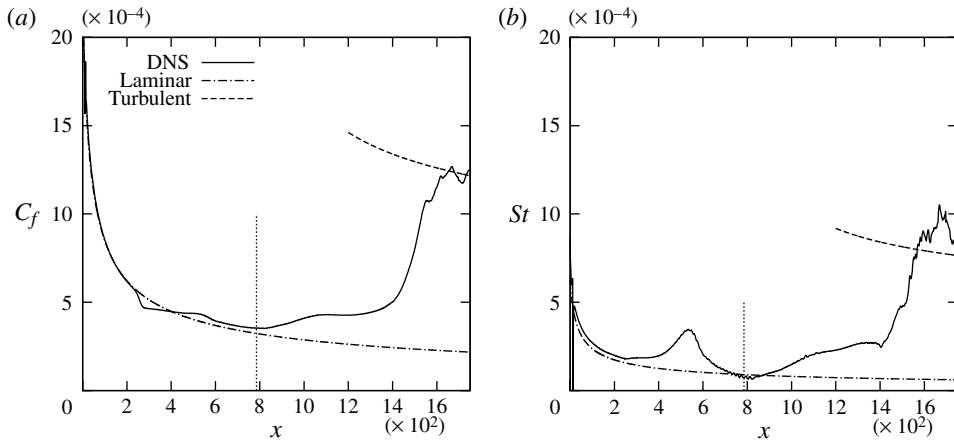

FIGURE 7. Skin friction coefficient and Stanton number averaged in span and time for the second mode fundamental resonance case. Turbulent correlations are computed from the Van Driest II and Reynolds analogy. Dotted vertical lines denote transition locations.

large magnitude of the two-dimensional instability wave and growth of oblique modes through fundamental resonance.

In the second mode oblique breakdown case, the skin friction and wall heat transfer minima occur earlier than in the second mode fundamental resonance case but breakdown occurs further downstream. Figure 8 shows the skin friction coefficient and Stanton number averaged over time and span as a function of the streamwise coordinate. Again, the skin friction and heat transfer increase and peak where the magnitudes of the primary instability waves peak before decaying. The transition location based on skin friction and wall heat transfer minimum are both at 784.8. The skin friction and heat transfer then rise gradually as the flow progresses downstream

FIGURE 8. Skin friction coefficient and Stanton number averaged in span and time for the second mode oblique breakdown case. Turbulent correlations are computed from Van Driest II and Reynolds analogy. Dotted vertical lines denote transition locations.

because of the breakdown of streaks generated by the initial instability (this is discussed further in §3.2). At $x = 1400$ the skin friction then rises rapidly and approaches the turbulent value. The Stanton number, however, rises less smoothly and spikes above the turbulent values. The small overshoot in heat transfer persists for approximately $150\delta^*_{in}$.

An increase in the growth of the boundary layer thickness is also commonly used as a definition of the boundary layer transition location because a turbulent boundary layer grows thicker faster than a laminar boundary layer. Behaviour of boundary layer thickness is shown in figures 9 and 10. For both the momentum and enthalpy thicknesses, the transition locations ($x_{tr,\theta}$ and $x_{tr,enth}$ respectively) are defined as the locations where the thickness measures depart 5 % from the laminar growth curve. The transition location based on this criterion is listed in table 4 and denoted in the figures using dotted vertical lines. Compared with the transition location based on the laminar skin friction value ($x_{tr,cf}$) shown in table 4, the increase in boundary layer growth occurs further downstream. For the first mode oblique breakdown case, the increase in growth of boundary layer thickness begins soon after the skin friction first departs from the laminar values and approximately $100\delta^*_{in}$ downstream of $x_{tr,cf}$. For the second mode fundamental resonance and second mode oblique breakdown cases, there are two locations where the boundary layer thickness growth changes. First, the boundary layer thickness growth begins to depart from the laminar values soon after the skin friction and heat transfer reach a minimum. Further downstream where the skin friction and heat transfer values approach the turbulent correlation values, the boundary layer growth suddenly increases. The first change in slope marks the start of transition and the second marks the termination of the transitional region. This again shows the extended transitional region for the second mode fundamental resonance and oblique breakdown cases which will be discussed further in the next section.

As the flow transitions from laminar to transitional to turbulent flow, energy moves from large scales to smaller scales. One way to track the transition of the flow to a turbulent state is through the turbulent energy spectrum. The spectrum in the spanwise direction is computed because the flow is homogeneous in this direction. To
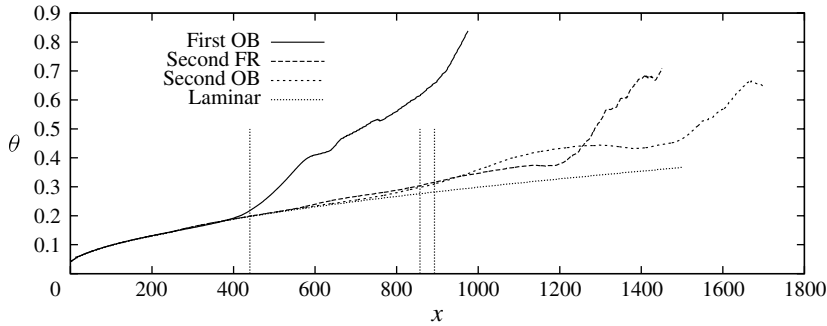
FIGURE 9. Momentum thickness for the three cases as a function of streamwise coordinate.
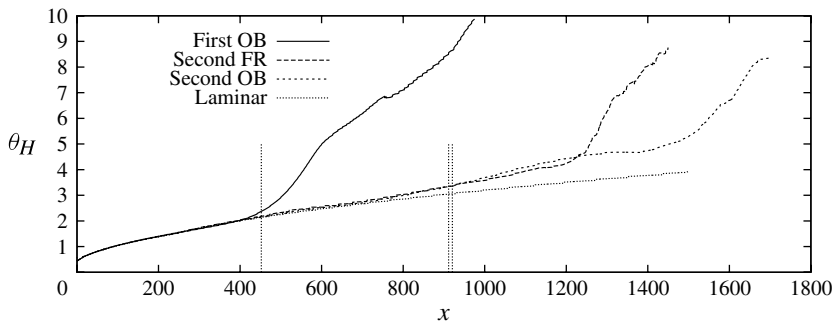

FIGURE 10. Enthalpy thickness for the three cases as a function of streamwise coordinate.

compute the energy in each velocity component, the Fourier transform ($\mathscr{F}_\alpha(x, y, \beta)$) in the spanwise direction is taken at a fixed x, y location for a specified spanwise wavenumber. The energy in each mode is then

$$E_{\alpha\alpha}(x, y, \beta) = \overline{\mathscr{F}_\alpha(x, y, \beta)\mathscr{F}_\alpha(x, y, \beta)}, \qquad (3.10)$$

where the over-line denotes an average in time and α represents a velocity component. Figure 11 shows the wall-normal integrated disturbance energy at a specified wavenumber of $\beta = 1.0$, for the spanwise velocity. A value of 0.0095, which is 95 % of the value in the turbulent region, is chosen as the transition location criterion. The transition location based on this criterion for the three cases can be found in table 4 labelled $x_{tr,end}$. In all three cases, this transition location is the furthest downstream of all of the criteria. This is expected because this measure is an indicator of the end of transition rather than the beginning of transition. In the first mode oblique breakdown case, the transition region is the shortest based on the spectrum criterion as the end of the transition region. For the Mack mode forcing cases, the disturbance energy for disturbances with $\beta = 1$ rapidly rises as the primary disturbances saturate and streaks are generated, but the turbulent value is not immediately reached. However, the flow does not fully break down until much further downstream. The transition location based on spanwise velocity disturbance energy at $\beta = 1.0$ for the second mode fundamental resonance and oblique breakdown cases matches with the second location where the boundary layer thickness slope changes. This again supports this location as the end of the transition region.
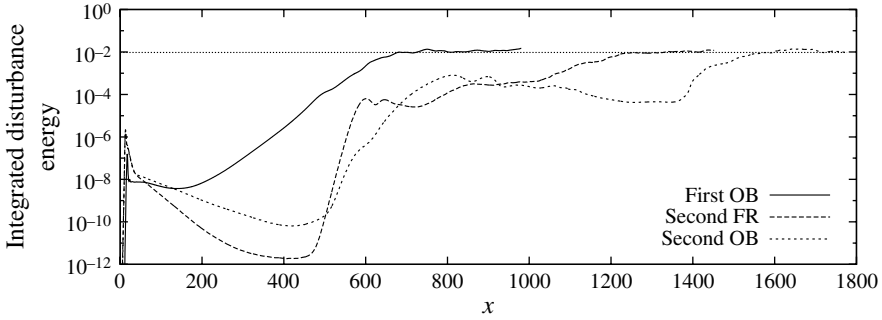
FIGURE 11. Disturbance energy of spanwise velocity for wavenumber of $\beta = 1.0$ integrated in the wall-normal direction.

The transition length is computed in table 4 using the initial transition location based on skin friction curve as the start of transition and the final transition location based on the spectrum criterion. The transition zone length corresponds to the transition location, i.e. the earlier the transition location, the shorter the transitional region. In experiments it has been generally observed that the transition location moves downstream and the transition zone is extended as the Mach number increases (Kimmel 1993). DNS computation of turbulent spots (Krishnan & Sandham 2006) showed that the spreading rate of the turbulent spots decreased with increasing Mach number.

3.2. *Modal growth during breakdown*

In this section, the details of the nonlinear breakdown process are discussed for the three different types of forcing. For all cases, the primary disturbances generate directly or indirectly streamwise streaks of low and high momentum/temperature. These streaks then break down to a fully turbulent flow.

To analyse the transition mechanism and the overshoot of heat transfer and skin friction, disturbance amplitudes are extracted based on frequency and spanwise wavenumber. The disturbance amplitudes are computed by first taking various snapshots in time of the flow field over one or more periods of the fundamental forcing frequency. Each flow field is then Fourier-transformed in both time and span. The amplitude of each mode is determined by the integration in the wall-normal direction of the disturbance energy as a function of the streamwise coordinate. The non-dimensionalized disturbance energy is defined as

$$E_{dist} = \int_0^{y_{max}} \frac{1}{2} \left(\bar{\rho} u_k' u_k' + \frac{\bar{T}}{\gamma \bar{\rho}} \rho' \rho' + \frac{\bar{\rho}}{\bar{T} \gamma (\gamma - 1)} T' T' \right) \, \mathrm{d}y. \tag{3.11}$$

Figure 12 shows selected mode amplitudes as a function of streamwise distance for the first mode oblique breakdown case. Each mode is denoted by frequency and spanwise wavenumber index $(\hat{\omega}, \hat{\beta})$, where $\hat{\omega} = 1$ denotes the frequency and $\hat{\beta} = 1$ denotes the fundamental spanwise wavenumber of the oblique waves which are forced. In the oblique case, the domain is three times as large as the fundamental wavelength of the oblique forcing. Only the modes $(1, 1)$ and $(1, -1)$ are intentionally forced, but other modes are excited at much lower amplitudes due to the shape and nature of the blowing and suction. The short dashed line shows the prediction of the growth of the $(1, \pm 1)$ oblique waves according to linear stability theory using the laminar base flow.
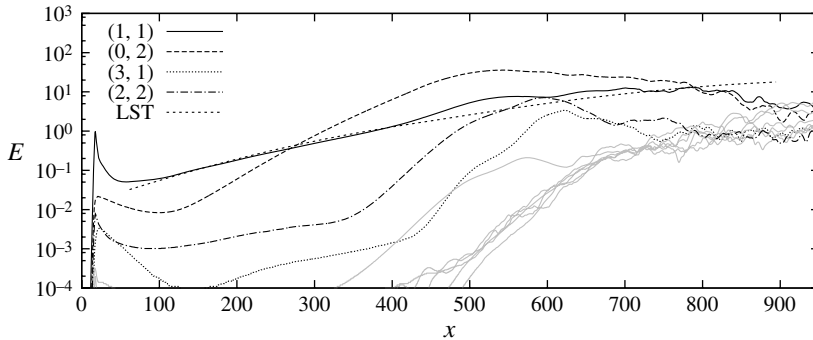
FIGURE 12. Disturbance energy content for modes (determined by frequency and spanwise wavenumber) as a function of streamwise coordinate for the first mode oblique breakdown case. Grey lines are higher unlabelled modes.

Initially the growth matches well, but once the amplitude of the disturbances becomes large, there are significant differences. There are two possibilities. The first is that because the mean flow has been changed by the large-amplitude fluctuations of the instability wave, linear stability theory should no longer predict the growth rate exactly. Another possibility is the existence of a secondary instability due to the modification of the mean flow from the large stationary disturbances caused by the interaction of the $(1, 1)$ and $(1, -1)$ modes. Because the modal decomposition is only based on frequency and spanwise number, it is impossible to determine whether the magnitude is due to the oblique waves initially forced or another instability introduced by the modification of the mean flow.

In the first mode oblique breakdown case, the initial breakdown is due to the interaction of the two oblique waves, which leads to the large growth of a stationary spanwise varying mode $(0, 2)$. This has been observed for previous oblique breakdown simulations for supersonic flow (Thumm *et al.* 1989; Mayer *et al.* 2011; Jiang *et al.* 2006). This $(0, 2)$ mode consists of streamwise vorticity and streaks of alternating high-momentum/low-temperature and low-momentum/high-temperature streaks. Figure 13 shows the development of the streamwise vortices and the streamwise streaks of temperature for y–z planes at different x locations. At $x = 550$, six pairs of counter-rotating vortices can be seen. The increased transport in the wall-normal direction of thermal energy and momentum due to this streamwise vorticity causes the overshoot of skin friction and heat transfer. This fact will be further supported by the Reynolds stresses and heat fluxes. Previously Xiong & Lele (2004) showed that heat transfer enhancement due to vortical disturbances in an incompressible Hiemenz boundary layer depended on the length scale of the disturbances. The maximum heat transfer enhancement occurred for disturbances with length scales approximately five times the boundary layer thickness. For the first mode oblique breakdown case, the disturbance length scale is approximately three times the boundary layer thickness where the heat transfer overshoot is observed. The work by Mayer *et al.* (2011) on oblique breakdown for a Mach 3.0 boundary layer had oblique disturbances with length scales approximately four times the boundary layer thickness in the breakdown region.

Once the streaks are generated, a secondary instability takes over and other modes are quickly introduced. The large vortices begin to break down at $x = 625$. At $x = 700$,
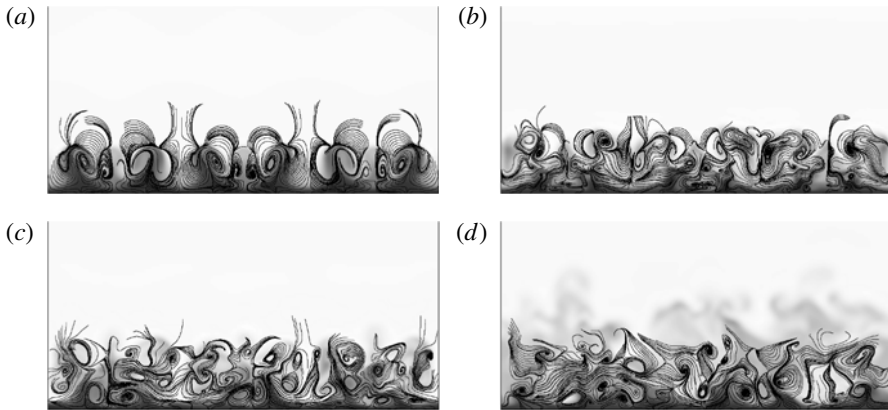
FIGURE 13. *y–z* planes with instantaneous streamlines and colour contours of temperature for the first mode oblique breakdown case: (*a*) *x* = 550; (*b*) *x* = 625; (*c*) *x* = 700; (*d*) *x* = 900.
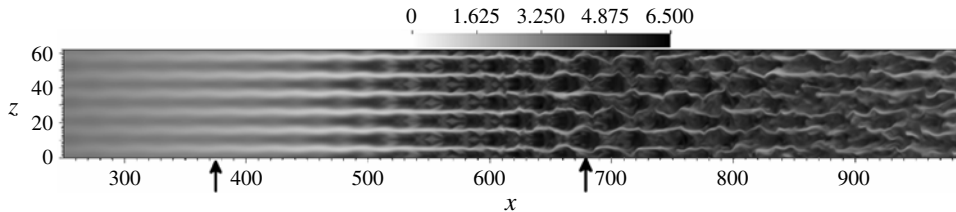

FIGURE 14. *x–z* plane at *y* = 2.5 with contours of streamwise velocity for the first mode oblique breakdown case. Arrows mark the beginning of transition based on skin friction and the end of transition based on spanwise velocity disturbance energy respectively.

a wide range of modes have significant amplitudes and the strong streamwise vortices have broken up. At the end of the domain, the flow contains the large range of scales characteristic of turbulent flows. The development and breakdown of the streaks can clearly be seen in figure 14. The streak instability appears to be of a sinuous nature and sinuous disturbances were also found to be the most unstable for optimal streaks in incompressible flows (Andersson *et al.* 2001). The *z*-displacement caused by the streak instability at first grows and then decays. This is because the most intense region of instability moves away from the wall as the flow develops downstream. The development of smaller scales and the chaotic motion of turbulence is evident in all of these figures.

To demonstrate that the large-amplitude forcing does not change the transition process significantly, the initial forcing amplitude of each of the oblique waves is decreased by a factor of 20. The modal decomposition is again undertaken and the modal development is compared with that of the initial forcing amplitude simulation. Figure 15 shows a comparison of the amplitudes of oblique modes (1, 1) and the initially excited nonlinear modes (0, 2), (3, 1) and (2, 2). The amplitudes of the primary oblique modes of the lower-amplitude forcing simulation are scaled up a factor of 20 to directly compare the modal development with the original simulation. The growth of the forced oblique modes (1, 1) is clearly linear until *x* = 400 for the high-amplitude forcing case. The low-amplitude forcing simulation, high-amplitude
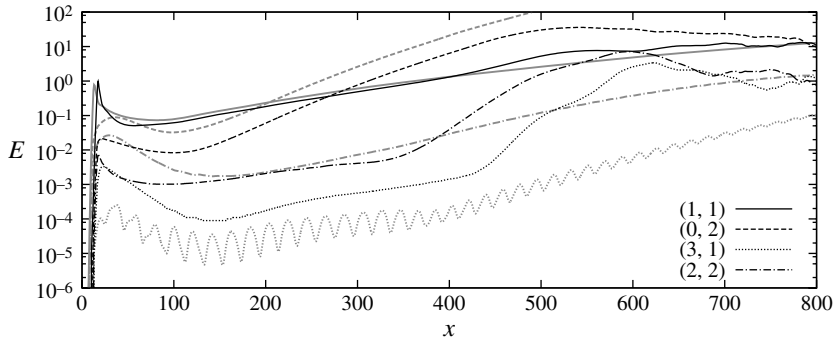
FIGURE 15. Disturbance energy content for modes (determined by frequency and spanwise wavenumber) comparing two different forcing amplitudes for the first mode oblique breakdown case. The black curves are original (higher-amplitude forcing) and the grey curves are lower-amplitude forcing rescaled.
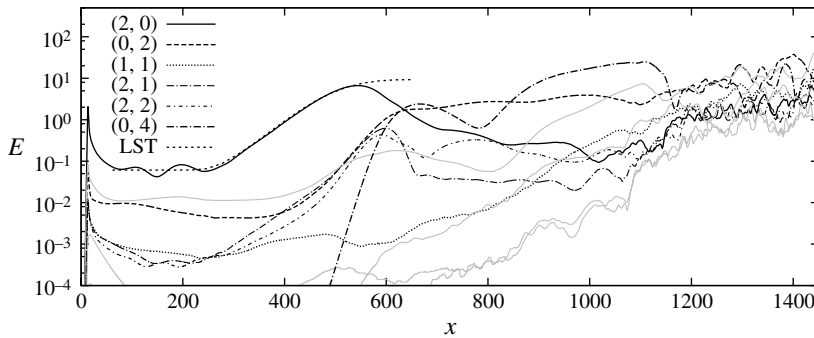

FIGURE 16. Disturbance energy content for modes (determined by frequency and spanwise wavenumber) as a function of downstream distance for the second mode fundamental resonance case.

forcing simulation, and linear stability theory all predict the same growth. The modes $(0, 2)$, $(3, 1)$ and $(2, 2)$ are scaled by a factor of 20^2 since they grow nonlinearly in both the high-amplitude forcing and the lower-amplitude forcing cases. They both grow with similar growth rates but their amplitudes do not scale directly with quadratic scaling. This may be caused by the receptivity process which is probably nonlinear due to the large-amplitude forcing. The initial portion (from the inlet until $x = 400$) of the high-amplitude forcing case can best be described as weakly nonlinear. The growth of the primary disturbances is still linear but other modes are excited through nonlinear effects. Modifying the forcing amplitude does not significantly change the transition process, and the high-amplitude initial forcing is justified. The effect of lower-amplitude forcing was also checked for the Mack two-dimensional and second mode oblique breakdown forcing cases and similar behaviour was observed (see Franko 2011). Therefore, results of the lower-amplitude forcing for these two cases are not included here.

Figure 16 shows the different modes for the second mode fundamental resonance case. The fundamental mode is denoted by $(2, 0)$, which is a two-dimensional
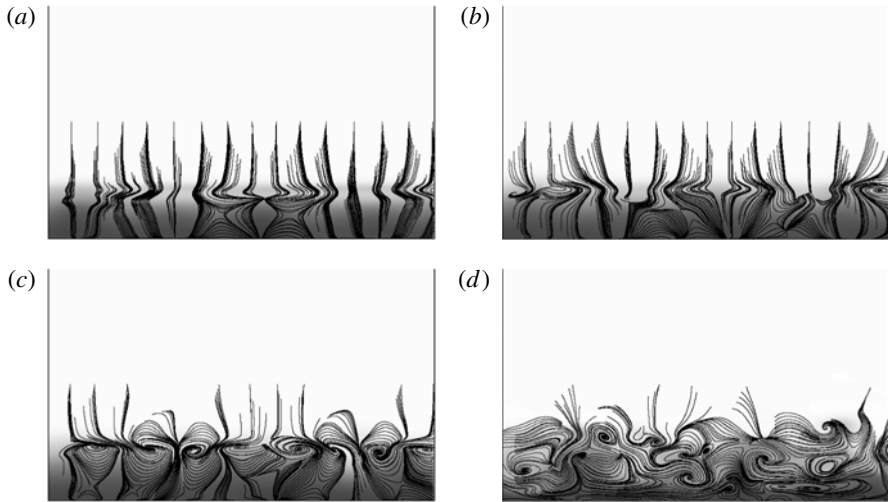
FIGURE 17. *y–z* planes with instantaneous streamlines and colour contours of temperature for the second mode fundamental resonance case: (*a*) $x = 650$; (*b*) $x = 750$; (*c*) $x = 850$; (*d*) $x = 1250$.

Mack mode. The growth of the $(2, 0)$ mode follows the growth predicted by linear stability theory until the mode amplitude becomes large and growth saturates. The linear stability prediction starts and ends relatively flat, because this mode is initially stable and is only unstable for a limited streamwise distance, which is characteristic of second mode instabilities. An additional linear stability theory calculation (not shown) was run using the mean flow of the DNS simulation as the base flow. It shows that the growth of the primary disturbance wave is significantly affected by the modification of the mean slow starting at $x = 500$. This demonstrates that the saturation is due to the modification of the mean flow rather than the transfer of energy between modes. The large amplitude of the fundamental mode produces the growth of oblique waves with the same fundamental frequency. The initial nonlinear mechanism is fundamental resonance. However, even though mode $(2, 1)$ grows large and there is growth of the $(0, 2)$ mode similar to that of the first mode oblique breakdown case, transition does not occur quickly based on the growth of higher harmonics and the development of the mean flow. Higher modes, shown in grey, do not grow large quickly and the boundary layer does not transition until $600\delta^*_{in}$ downstream of the saturation location of the primary two-dimensional second mode instability. The growth of oblique modes through fundamental resonance generates vorticity which leads to the generation of streaks as well as the first peak in heat transfer and skin friction. The vorticity generated in this case is weaker. It must be emphasized that the $(0, 2)$ mode in this case and the $(0, 2)$ mode in the oblique breakdown case are not the same. The stationary mode $(0, 2)$ has different spanwise wavenumber and a much lower amplitude than in the first mode oblique breakdown case which can be seen by comparing the amplitude of the streaks in figures 12 and 16 or figures 13 and 17. While the spanwise wavenumber may affect the growth rate of secondary instabilities of the streaks, the amplitude of the streaks is the most important parameter. The interaction of first mode oblique disturbances leads to strong vortices and strong streaks that quickly break down. The streaks generated in the second mode
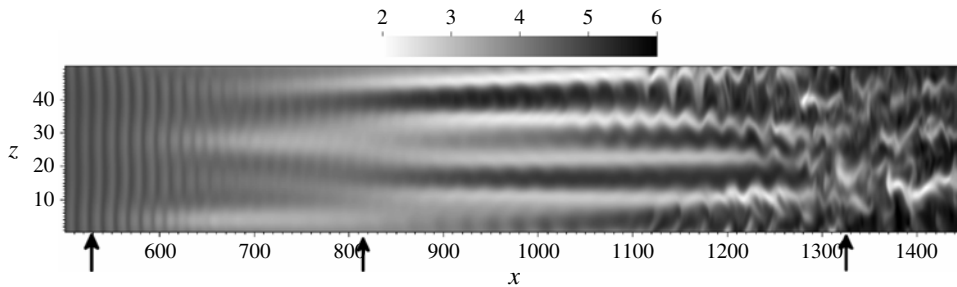
FIGURE 18. Two-dimensional slice of contours of streamwise velocity at $y = 4.5$. Initially two-dimensional Mack instabilities, then streaks, and eventually breakdown can be seen. Arrows mark the beginning of transition based on skin friction, saturation of the primary Mack second mode disturbance, and the end of transition based on spanwise velocity disturbance energy respectively.

fundamental resonance forcing case are initially weaker, grow larger downstream and eventually are large enough to lead to breakdown. Figure 17 shows the development of the streamwise vortices and the streamwise streaks of temperature for the second mode fundamental resonance case within y–z planes at different x locations. Figure 18 shows the development of the streamwise velocity streaks for an x–z plane located at $y = 4.5$. Immediately after the saturation of the primary two-dimensional second mode disturbance at $x = 650$, the three-dimensionality of flow is very low. As the flow develops downstream, vortices begin to grow near the boundary layer edge and eventually the flow begins to break down at the end of the domain. The long region of transitional flow was also observed for a DNS computation by Koevary *et al.* (2010) of Mach 8 flow over a sharp cone excited in a similar manner.

Figure 19 shows the amplitude of different modes for the second mode oblique breakdown case. The fundamental oblique second modes are $(1, \pm 1)$. The growth of the $(1, 1)$ mode follows the growth predicted by linear stability theory until the amplitude of the mode is large. In both the second mode fundamental resonance and three-dimensional cases, the primary instability mode amplitude saturates. This is shown by comparison with linear stability theory and low-amplitude forcing (see Franko 2011). The two oblique modes do generate the stationary streamwise modes $(0, 2)$ and $(0, 4)$ present in the first mode oblique breakdown scenario, but at a much lower amplitude. The explanation for the prolonged transitional region is the same as in the second mode fundamental resonance case. The streak amplitudes are initially too low to lead to immediate breakdown. Once the streaks grow large enough, breakdown occurs near the end of the domain. In the second mode oblique breakdown case, the strength of these stationary modes persists until the end of the domain (see figure 20). Pruett & Chang (1995) computed transition caused by two oblique Mack modes as well and observed the generation of a strong stationary mode, streaks and a protracted transitional region. Computational cost prevented them from obtaining complete breakdown or a fully turbulent flow.

In all three of the forcing cases explored in this work, streamwise streaks are generated and eventually break down to turbulence. However, the nature of streaks excited and the breakdown process differ. Previously for incompressible flows, detailed studies of streak breakdown (Andersson *et al.* 2001; Brandt & Henningson 2002; Hœpffner, Brandt & Henningson 2005) have been undertaken. In incompressible
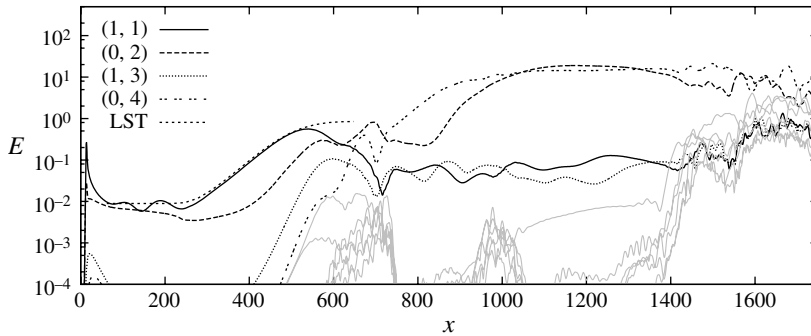
FIGURE 19. Disturbance energy content for modes (determined by frequency and spanwise wavenumber) as a function of downstream distance for the second mode oblique breakdown case.
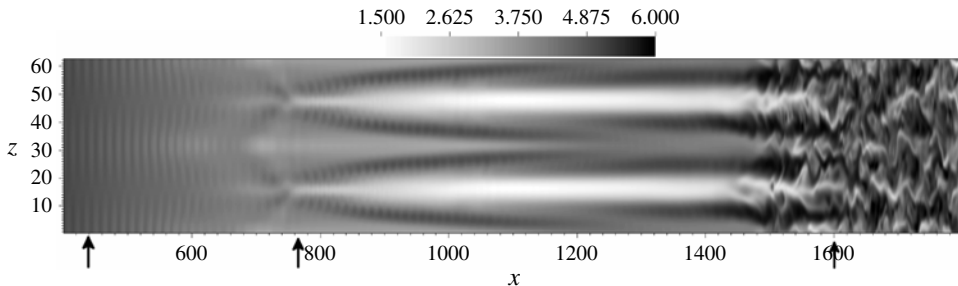

FIGURE 20. Two-dimensional slice of contours of streamwise velocity at $y = 4.5$. Initially three-dimensional Mack instabilities, then streaks, and eventually breakdown can be seen. Arrows mark the beginning of transition based on skin friction, saturation of the primary Mack second mode disturbances, and the end of transition based on spanwise velocity disturbance energy respectively.

flows, the most important parameter that determines breakdown is the strength of the streaks. Andersson *et al.* (2001) studied secondary instability due to optimal streaks in incompressible boundary layer flow. The threshold for secondary instability of streaks was 26 % of the free stream velocity and the growth rate of secondary instabilities scaled with the amplitude of the streaks. Cossu *et al.* (2011) studied the streak and sinuous secondary instability amplitude combinations needed for breakdown of optimal streaks in plane Couette and Blasius boundary layer flows. Using DNS, they were able to map a two-dimensional plane of the combined threshold needed for both amplitudes. They concluded that not only did the streak amplitude matter but the amplitude of the secondary streak instability was also important.

In the current cases, analysis of the streak breakdown mechanisms is limited due to the uncontrolled generation of the streaks. In addition, the three cases investigated here are too limited to make a two-dimensional map of the streak and secondary instability amplitudes required for complete breakdown. However, some insight can be obtained by studying the structure of the streaks generated, their amplitude and their eventual breakdown. Figures 14, 18 and 20 show instantaneous snapshots of the streaks in *x–z* plans for the three cases. In all three cases, sinuous secondary instability of the streaks
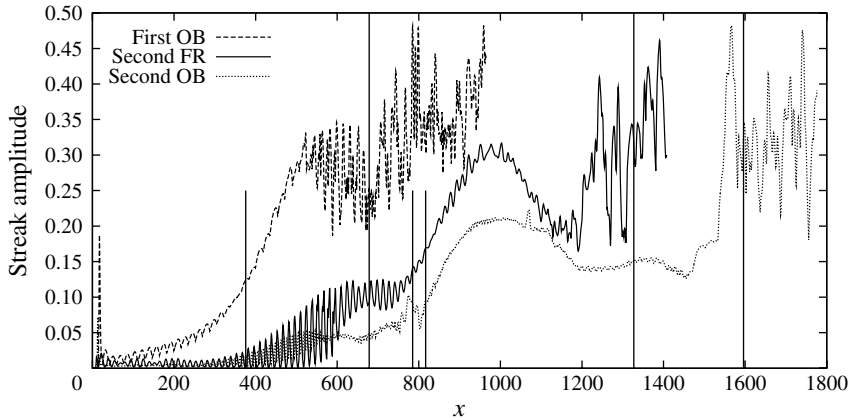
FIGURE 21. Instantaneous streak magnitude. The short vertical black lines denote the beginning of transition region for the first mode oblique breakdown, second mode fundamental resonance, and second mode oblique breakdown forcing cases respectively. The long vertical black lines denote the end of the transition region based on the energy of the spanwise velocity fluctuations.

leads to the breakdown to transition. In the second mode fundamental resonance and three-dimensional cases, the process is more gradual and the streaks persist longer, probably because of their weaker initial amplitude. Interestingly, once a secondary instability has been generated, the process can become self-sustaining (Cossu *et al.* 2011). The secondary instability creates streamwise vorticity which strengthens the streaks, leading to further secondary instability. Evidence of this can be seen in the series of *y–z* views in figure 17. Also, the continued growth of the stationary modes in figures 16 and 19 may be evidence of this.

The breakdown of the streaks can be analysed in a more quantitative way as well. Because both the streak amplitude and secondary instabilities are important, both need to be considered. Extracting the streak amplitude and secondary streak instability amplitude are difficult in these computations because of the uncontrolled generation of streaks. Previous studies (Andersson *et al.* 2001; Hœpffner *et al.* 2005; Cossu *et al.* 2011) of streak breakdown have started with streaks generated in a controlled fashion. In the present work, the streak amplitude definition of Andersson *et al.* (2001) is used:

$$A = \frac{1}{2U_\infty} \left[\max_{y,z}(U - U_B) - \min_{y,z}(U - U_B) \right]. \tag{3.12}$$

The maximum r.m.s. values of the spanwise velocity fluctuations are extracted and used as a surrogate of the secondary instability of the streaks. Figures 21 and 22 show the development of the streak amplitude and spanwise velocity fluctuations for the three different cases. The short vertical lines denote transition location based on minimum skin friction coefficient and the long vertical lines denote approximate breakdown location based on the spectrum criteria in § 3.1. For all of the cases, the maximum streak amplitudes are similar to those of previous incompressible studies of controlled streak generation and instability (Andersson *et al.* 2001; Hœpffner *et al.* 2005; Cossu *et al.* 2011). For the first mode oblique breakdown case, both the streak amplitude and spanwise velocity fluctuations are large in the transitional region due to the growth of the oblique modes and the resulting streamwise vortices that are
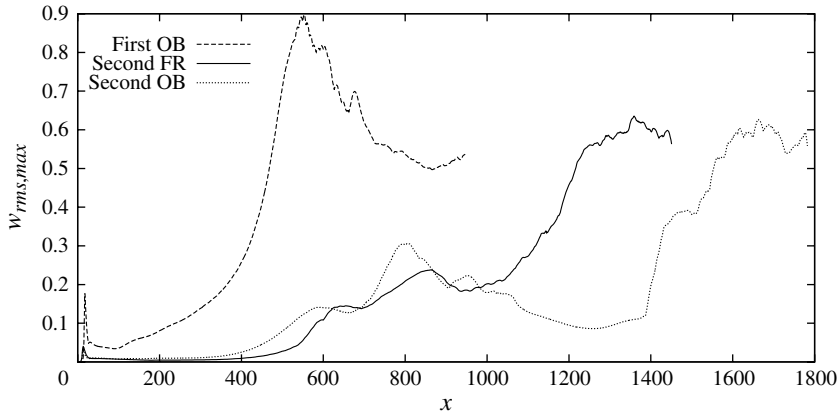
FIGURE 22. Maximum r.m.s. value of spanwise velocity fluctuations as a function of streamwise coordinate.

generated. In both the second mode fundamental resonance and oblique breakdown cases, the streak amplitude grows after the saturation of the primary instability wave. The spanwise velocity fluctuations are smaller than in the first mode oblique breakdown case until the flow is fully turbulent. For the second mode fundamental resonance case, the streak amplitude reaches the same value as in the first mode oblique breakdown case but further downstream and after the saturation of the primary two-dimensional disturbance. Starting at $x = 1000$, the spanwise velocity fluctuations increase in an amplitude and further downstream, complete breakdown occurs. For the second mode oblique breakdown case, the maximum amplitude of the streaks generated is smaller than in both the first mode oblique breakdown and second mode fundamental resonance cases. The streaks persist at a nearly constant amplitude until $x = 1400$ when the spanwise velocity fluctuations increase and soon after the complete breakdown occurs. In these three cases, it is evident that large-amplitude streaks are generated and their secondary instability eventually leads to complete breakdown. In all three cases, the measure of streak amplitude and the maximum of the spanwise velocity fluctuations approach the same value in the turbulent region.

3.3. *Wall cooling*

For hypersonic flows, solid surfaces typically have lower temperatures than the adiabatic wall temperature. As the wall temperature is lowered, the growth rates and N factors for first mode disturbances will decrease and the growth rates and N factors for second mode disturbances will increase. Masad (1993) studied in detail the effect of wall temperature ratios on the N factors for Mach numbers similar to those studied here. As the temperature decreases, second mode disturbance growth dominates first mode disturbance growth.

Two additional simulations of the second mode fundamental resonance were undertaken to demonstrate that qualitatively the nonlinear stage of the transition process for second mode disturbances does not change as the wall temperature is decreased. Table 5 gives a summary of these two additional simulations. The amplitude, frequency, and spanwise wavenumbers of the primary and secondary disturbance waves for each case are included in this table. The increased cooling of the wall has no effect on the transition and breakdown mechanism for the second
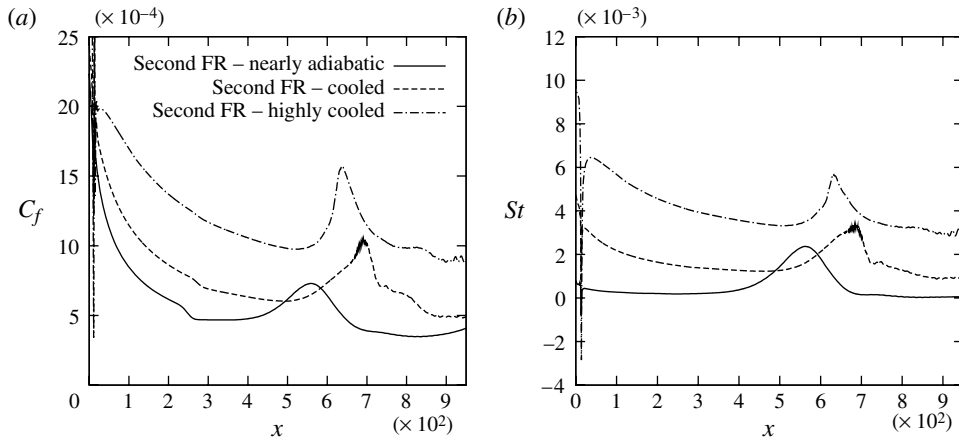
FIGURE 23. Skin friction coefficient and Stanton number averaged in span and time for the second mode fundamental resonance cooled and highly cooled cases.
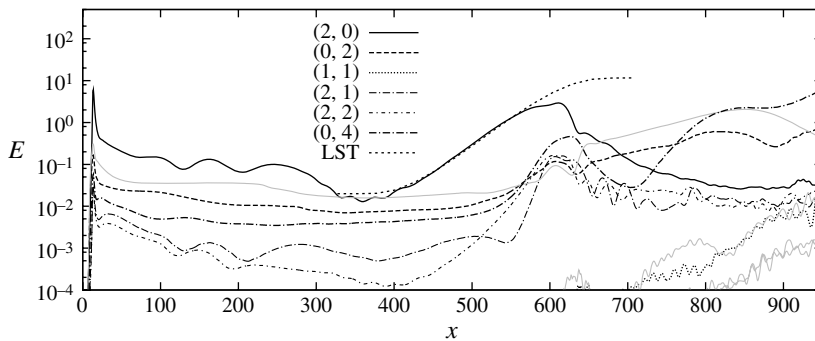

FIGURE 24. Disturbance energy content for modes (determined by frequency and spanwise wavenumber) as a function of downstream distance for the second mode fundamental resonance highly cooled.

mode fundamental resonance mechanism. Figure 23 shows the skin friction coefficient and Stanton number averaged in time and span for the two cooled wall cases and the isothermal nearly adiabatic case. The two cooled cases follow the same pattern as the nearly adiabatic wall case discussed in § 3.1. The skin friction and heat transfer both increase and initially peak where the primary two-dimensional disturbance saturates and oblique modes grow rapidly through fundamental resonance. The saturation of the primary disturbance wave for the highly cooled case can be seen in figure 24. Because the N factors are higher for second mode instabilities with cooler walls, the saturation occurs well below the peak amplitude predicted by linear stability theory. The saturation of the primary second mode instabilities was observed in all cases. In both cooled wall cases, the primary disturbances saturate and streaks are generated which do not immediately break down. The domain is too short to capture the complete breakdown of the streaks to turbulence but the saturation, fundamental resonance, and streak generation do not qualitatively change with wall cooling.

Case	Second mode FR cooled	Second mode FR highly cooled
x_{max}	1000	1000
y_{max}	50	50
z_{max}	50.27	50.27
nx	1536	1536
ny	150	150
nz	64	64
T_w/T_e	4.0	2.5
ω	2.4	2.7
$A_{primary}$	$0.1U_e$	$0.1U_e$
$A_{secondary}$	$0.005U_e$	$0.005U_e$
$\beta_{secondary}$	0.125, 0.25, 0.5	0.125, 0.25, 0.5

TABLE 5. Summary of DNS computations of transition.

3.4. *Skin friction and heat transfer overshoot*

Previously, plots of skin friction and wall heat transfer coefficients were shown for all three cases. The first mode oblique forcing leads to the earliest transition location along with a clear overshoot in skin friction and heat transfer. The mechanism for this has been alluded to, but will be discussed in more detail in the current section along with further discussion of the wall heat transfer and correlations used. Analysis of the wall heat transfer for the second mode fundamental resonance and three-dimensional cases is also included.

The large skin friction and heat transfer overshoots in the first mode oblique breakdown case (shown in figure 6) are caused by the interaction of the two oblique instability modes. The two instability modes generate streamwise vorticity which transport momentum and thermal energy vertically through the boundary layer. The complete transition process was described in the previous section using the modal decomposition. The wall Stanton number averaged in time as a function of the streamwise and spanwise coordinates (x, z) shown in figure 25 provides further evidence of this mechanism. At the same location where there is an overshoot in heat transfer, there is a clearly defined pattern of the wall heat transfer in the spanwise direction. The Stanton number is sinusoidal with a wavenumber twice the fundamental forcing spanwise wavenumber of the two oblique waves, the same wavenumber as the stationary disturbance. A similar pattern can be seen in the skin friction except that the streaky structures persist longer (see Franko 2011). The shape of the skin friction and wall heat transfer in the transitional region can be explained using this figure as well as figure 13. The initial increase in skin friction and heat transfer is due to the streamwise vorticity generated by the interaction of the two primary oblique instability waves. Between $x = 550$ and $x = 600$, there is a small plateau in the skin friction that is caused by the initial breakdown of the strong counter-rotating vortices. The skin friction and wall heat transfer then continue to rise beyond the turbulent correlation as the streamwise vorticity and streaks continue to break down. The wall heat transfer and skin friction finally match with the turbulent correlations as the flow becomes fully turbulent.

In the turbulent region (from $x = 750$ to the end of the domain) the heat transfer is lower than the turbulent correlation, as seen in figure 6. The turbulent correlation depends on the Van Driest II correlation for skin friction and the Reynolds analogy,
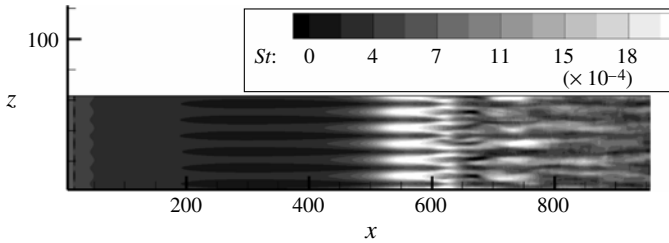
FIGURE 25. Wall heat transfer (Stanton number) averaged in time for the first mode oblique breakdown case.
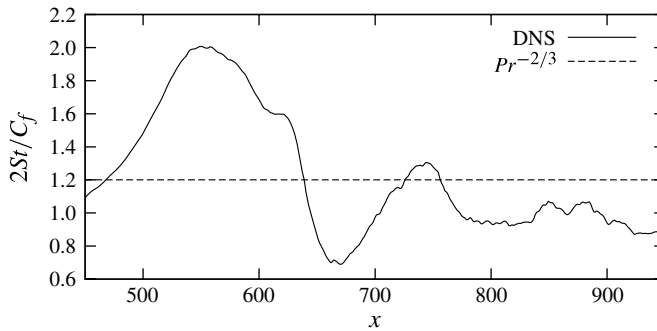

FIGURE 26. Reynolds analogy factor ($2St/C_f$) compared with $Pr^{-2/3}$ in the transitional and turbulent regions for the first mode oblique breakdown case.

which depends on the chosen Reynolds analogy factor. Figure 26 shows the Reynolds analogy factor ($2St/C_f$) in the transitional and turbulent regions. Even though there is overshoot in both skin friction and heat transfer, the Reynolds analogy does not hold in the transitional region. The heat transfer is higher than would be expected if the Reynolds analogy held. The value of the Reynolds analogy factor for high-speed flows is not clear. Reynolds analogy factor values between 0.9 and 1.2 have been suggested by (Hopkins & Inouye 1971; Bradshaw 1977; Roy & Blottner 2006) based on experimental results. In the turbulent region for the first mode oblique breakdown case, the value of the Reynolds analogy factor is close to 1.0. The value used for the Reynolds analogy factor for the heat transfer correlation in figure 6 is $Pr^{-2/3} \approx 1.2$. If a lower value were used for the Reynolds analogy factor, the agreement between turbulent correlation and simulation in the turbulent region would be much better.

By plotting the skin friction and heat transfer as a function of x, the comparison to the turbulent semi-empirical correlations is arbitrary because a virtual origin must be chosen. One alternative is to plot the skin friction and heat transfer as functions of the momentum thickness Reynolds number (Re_θ), as suggested Fernholz & Finley (1996) (O. N. Ramesh, personal communication, 2010) to potentially eliminate the observed overshoot. This is done by transforming an incompressible turbulent correlation to a compressible quantity (Hopkins & Inouye 1971). The incompressible correlation used is Blasius:

$$C_{f,inc} = \frac{0.026}{Re_{\theta,inc}^{1/4}}. \tag{3.13}$$
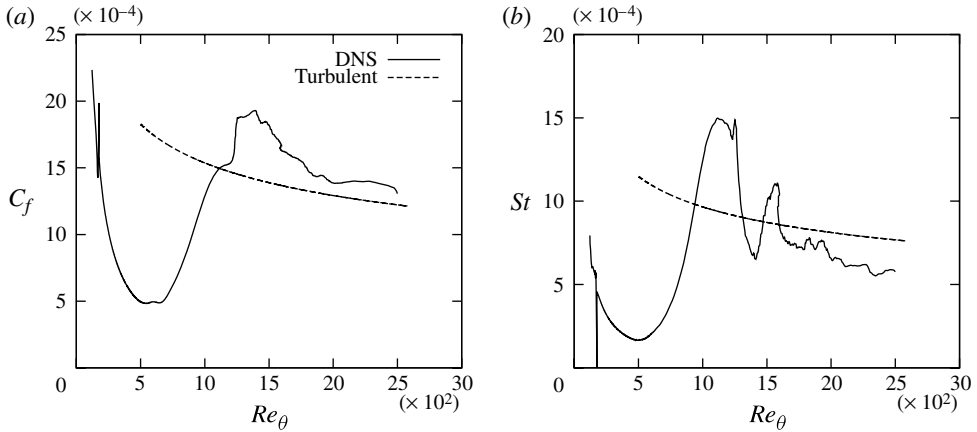
FIGURE 27. Skin friction coefficient and Stanton number averaged in span and time for the first mode oblique breakdown case. Turbulent correlations are computed from the semi-empirical Van Driest II correlation and the Reynolds analogy.

To transfer between the incompressible and compressible correlations, the following relations are used:

$$C_{f,inc} = F_c C_f, \quad Re_{\theta,inc} = F_\theta Re_\theta. \tag{3.14}$$

For Van Driest II:

$$F_\theta = \frac{\mu_e}{\mu_w} \quad F_c = \frac{r\dfrac{\gamma - 1.0}{2}M_e^2}{(\sin^{-1}A + \sin^{-1}B)^2}. \tag{3.15}$$

Figure 27 shows both the skin friction coefficient and Stanton number plotted versus Re_θ along with the Van Driest II correlation. Clearly, both the skin friction and heat transfer still overshoot the turbulent values in the transitional region. Plotting versus Re_θ does not eliminate the observed overshoot. The discrepancy in the turbulent region, particularly for the skin friction curve, is probably due to the low Reynolds number. When Re_θ is converted to $Re_{\theta,inc}$, the resulting Reynolds number is low and near the limit of applicability for the incompressible correlation.

Figure 28 shows the heat transfer (Stanton number) at the wall averaged in time as a function of streamwise distance and span for the second mode fundamental resonance case. The peak in Stanton number is due to the large magnitude of the two-dimensional instability mode near $x = 550$, which leads to nearly constant heat transfer across the span. There is some three-dimensionality introduced as this first peak decays. In the transitional region, there are no clearly defined structures as in the case of first mode oblique breakdown. Also, in contrast to the first mode oblique transition scenario, the breakdown process does not occur rapidly. For both the second mode fundamental resonance and second mode oblique breakdown cases, there is a large increase in wall heat transfer as the second mode instability grows large and saturates. The wall heat transfer then drops back towards the laminar values before increasing as the boundary layer completely transitions further downstream. This pattern of heat transfer was recently observed experimentally in a quiet Mach 6 wind tunnel on a flared cone (Chou *et al.* 2011). Because a flared cone is used, it is possible that Görtler vortices are responsible for the streaky heat transfer pattern
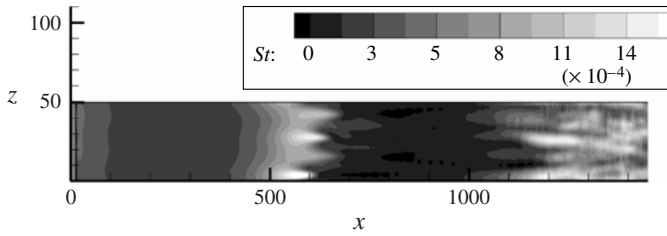
FIGURE 28. Wall heat transfer (Stanton number) averaged in time for the second mode fundamental resonance case.
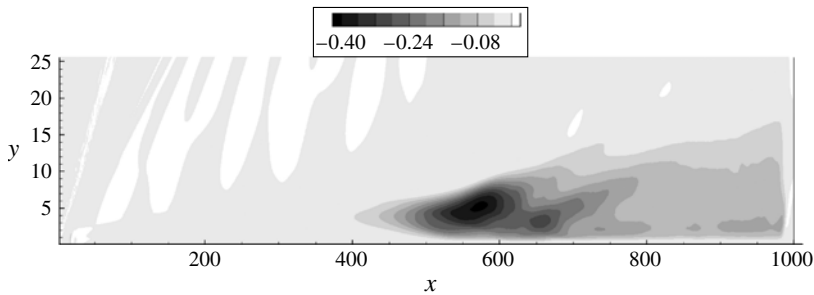

FIGURE 29. Contours of $\overline{\rho u'' v''}/\rho_w U_e U_e$ for the first mode oblique breakdown case. The scale for the y-axis has been magnified by a factor of 10.

but the growth of the primary instability wave and generation of higher-frequency disturbances in the experiment suggest that the mechanisms in the experiment and the present computation are similar.

In the transitional region of the first mode oblique breakdown case, the Reynolds shear stress and Reynolds heat flux terms responsible for the transport of momentum and thermal energy away from the wall are analysed. Figure 29 shows the Reynolds shear stress, $\overline{\rho u'' v''}/\rho_w U_e U_e$. The Reynolds shear stress in the boundary layer is negative. Negative values mean that high-momentum fluid is moved towards the wall and low-momentum fluid is moved away from the wall. This transport of momentum leads to an increase in skin friction. The large negative values of $\overline{\rho u'' v''}/\rho_w U_e U_e$ occur between $x = 550$ and $x = 750$, which correspond to the overshoot in skin friction (see figure 6). Figure 30 shows the quantity $\overline{\rho v'' T''}/\rho_w U_e T_w$, which is the wall-normal component of the Reynolds heat flux. Positive values mean that high-temperature fluid is moved away from the wall and low-temperature fluid is moved towards the wall. The transport of thermal energy leads to an increase in wall heat transfer. The main peak of $\overline{\rho v'' T''}/\rho_w U_e T_w$ occurs between $x = 550$ and $x = 600$, which corresponds to the first overshoot in heat transfer (see figure 6). The additional peaks in heat transfer also match with the peaks in wall-normal Reynolds heat flux. The values of both Reynolds stress and Reynolds heat flux approach nearly constant values as the boundary layer fully develops. The drop-offs near the end of the domain are due to the sponge boundary condition located at the outflow.

In all three cases, the shape of the rise in skin friction and heat transfer is not due to intermittency but rather the specific transition mechanisms in each case. Because the forcing in all cases is strictly periodic in time, there are no turbulent
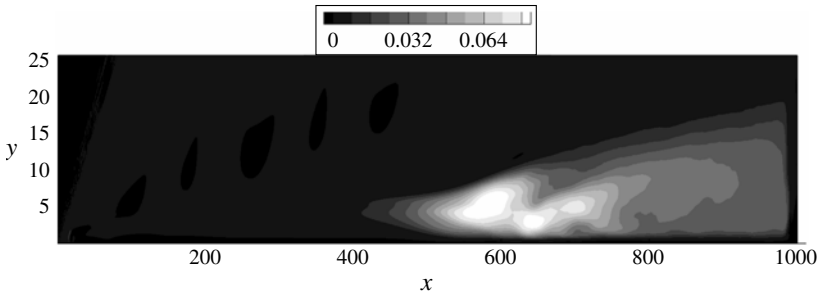
FIGURE 30. Contours of $\overline{\rho v'' T''}/\rho_w U_e T_w$ for the first mode oblique breakdown case. The scale for the y-axis has been magnified by a factor of 10.

spots or intermittency (Kachanov 1994). In 'natural' or uncontrolled conditions, typical of flight and experiments, the background disturbances are more random, and intermittency and turbulent spots are produced. Narasimha (1985) reviews the physics and modelling of the transition region with a focus on intermittency and the generation of turbulent spots. The intermittency approach blends laminar and turbulent values $(C_f = \gamma C_{f,turb} + (1 - \gamma) C_{f,lam})$ to compute the skin friction and heat transfer in the transitional region and the overshoot can be modelled if the dependence on Reynolds number is different for the turbulent values (Dhawan & Narasimha 1958).

Although true intermittency does not exist in the present simulations, two different measures that are surrogates for intermittency, which measure the progression from laminar to turbulent flow, were computed. The first is the based on the maximum turbulent spanwise velocity r.m.s. fluctuations scaled by the same quantity at the end of the domain:

$$\gamma_1(x) = \frac{\max_{y,z} w'_{rms}(x)}{\max_{y,z} w'_{rms}(x_{max})}. \tag{3.16}$$

The second measure (γ_2) is based on the spanwise velocity fluctuating energy at a set spanwise wavenumber of $\beta = 1$. Basically, the curves from figure 11 are clipped and scaled in order to obtain a parameter which begins at 0 and ends at 1. For this, the wall-normal integrated disturbance energy of the spanwise velocity is clipped so that 10^{-6} corresponds to $\gamma_2 = 0$ and 10^{-2} corresponds to $\gamma_2 = 1$, and in between those extremes it is scaled based on its log value.

Figure 31 shows the two intermittency measures and the modelled skin friction based on these intermittency measures. For the modelled skin friction, the two intermittency measures are used to blend the laminar and turbulent correlation described in §3.1. The turbulent correlation is the same used in figure 6. There is a discontinuity in the modelled skin friction based on the first intermittency measure because the turbulent skin friction is not defined before the virtual origin, and the intermittency is not small at the virtual origin. As described in §3.1 and table 4, the virtual origin for turbulent C_f correlation is taken as $x_{tr,Cf}$. The measure γ_1, based on maximum spanwise velocity r.m.s. fluctuations, matches the skin friction shape well but leads the skin friction curve. Note that γ_1 is a not a monotonic function of x, a reminder that it is not a true intermittency metric. The overshoot of the skin friction appears to be qualitatively captured by this intermittency surrogate, but it again leads the actual skin friction. The second intermittency surrogate γ_2, based on spanwise velocity disturbance energy, lags the skin friction and increases monotonically as
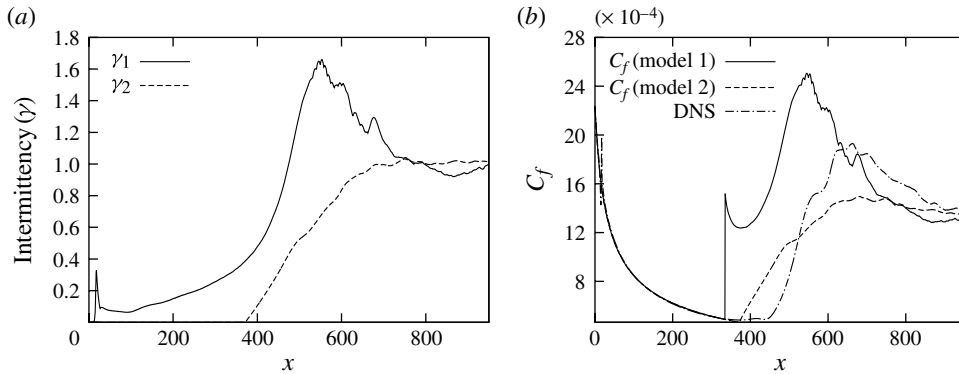
FIGURE 31. Intermittency measures and comparison of actual skin friction and modelled skin friction: (*a*) intermittency; (*b*) C_f.
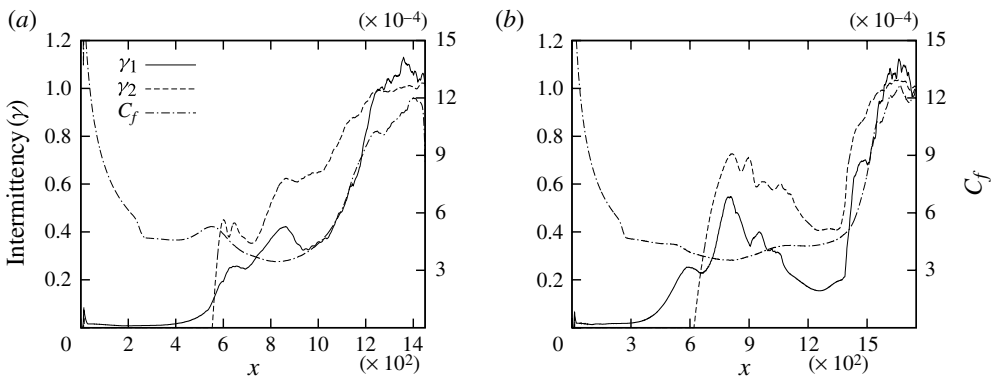

FIGURE 32. Intermittency measures compared with skin friction curves for second mode fundamental resonance and three-dimensional cases: (*a*) second mode fundamental resonance; (*b*) second mode oblique breakdown.

expected for true intermittency, but the C_f model based on γ_2 fails to show any overshoot behaviour.

Figure 32 shows these two measures of intermittency along with the development of the skin friction for the second mode fundamental resonance and three-dimensional cases. Both measures of intermittency track each other well, especially their shape, but do not match with the intermittency implied by the skin friction curve. The intermittency values are too high in the region where the streaks are growing but have not yet broken down.

3.5. *Turbulent flow development*

In addition to the evidence of turbulent flow development provided by the skin friction/wall heat transfer and boundary layer thickness, other measures demonstrate the progression to turbulent flows in the three different forcing cases. Because of the controlled discrete instability modes introduced into the initially laminar boundary layer and the resulting transition process, a fully turbulent flow with perfect statistics
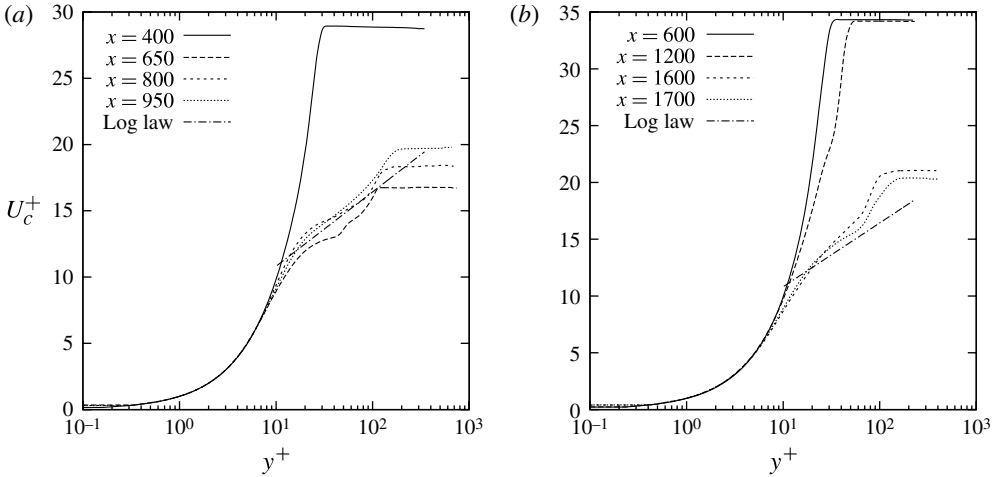
FIGURE 33. Wall scaled turbulent mean velocity at different x locations for the first mode oblique breakdown and second mode oblique breakdown cases.

should not be expected. However, the mean flow profiles, turbulent fluctuating quantities, spanwise turbulent spectrum, and the turbulent kinetic energy budget demonstrate a clear progression to a fully turbulent flow. The first mode oblique breakdown case is the most fully developed by the end of the domain due to its earlier transition location and more rapid breakdown process.

As the flow develops from laminar to turbulent flow, the mean profile should develop from that of a laminar boundary layer to that of a turbulent boundary layer. The velocity profile and wall-normal coordinate (y) are scaled based on the friction velocity (u_τ) and the viscous length scale (δ_w). Variables scaled in this way are denoted by a superscript $+$. The Van Driest transform is used for a compressible turbulent boundary layer to compare log law for incompressible boundary layer flows:

$$U_c = \int_0^{\bar{u}} \sqrt{\frac{\bar{\rho}}{\bar{\rho}_w}}\, \mathrm{d}u. \tag{3.17}$$

The mean flow profile should match the viscous sublayer ($y^+ = U_c^+$) near the wall (for $y^+ < 10$) and match the log law for larger $y+$ values:

$$U_c^+ = \frac{1}{\kappa} \ln(y^+) + C \quad \text{where } \kappa = 0.41, C = 5.2. \tag{3.18}$$

Figure 33(a) shows the scaled streamwise velocity mean profile for the oblique breakdown case at different streamwise locations. At $x = 400$, the flow is fully laminar and has the expected shape for a laminar flow. Once the boundary layer begins to transition ($x = 650$ and $x = 800$), the mean matches closer to the expected turbulent streamwise velocity profile but still does not match well in the log-law region. At $x = 950$, the mean flow matches with the expected turbulent streamwise mean velocity profile in both the viscous sublayer and the log-law region. At the end of the domain the mean flow appears to be fully turbulent.

Figure 33(b) shows the mean flow profiles for the second mode oblique breakdown case. Early in the boundary layer development ($x = 600$ and $x = 1200$) the boundary
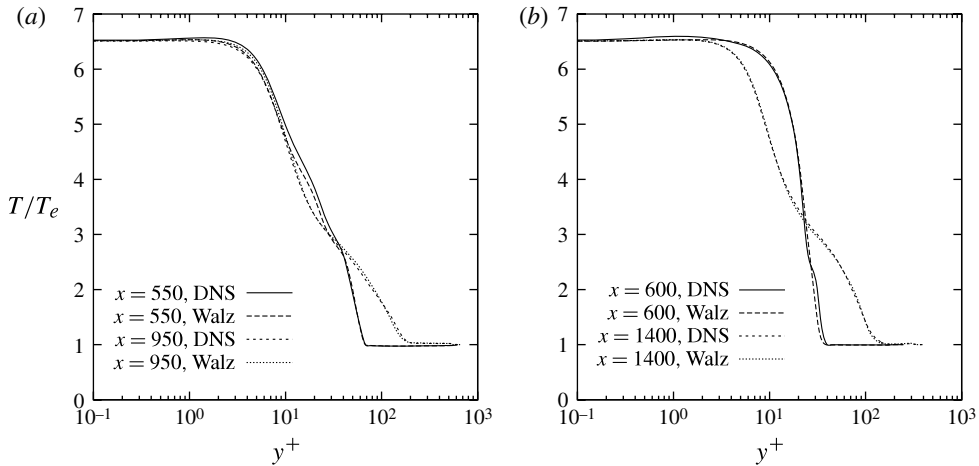
FIGURE 34. Favre-averaged temperature compared with Walz's equation at different x locations: (a) first mode oblique breakdown; (b) second mode fundamental resonance.

layer is nearly laminar. The large growth of the primary instability waves leads to a modification of the flow, but does lead to complete breakdown immediately. Further downstream, the boundary layer begins to transition ($x = 1600$), but by the end of the domain ($x = 1700$) the flow is still not fully turbulent, according to the mean streamwise velocity profile, because it does not match the log law. This is also supported by the value of skin friction, as seen in figure 8. The transitional region for this case is extremely long and at the end of the domain the flow is still developing to turbulence. The mean flow profiles for the second mode fundamental resonance case are not shown here (see Franko 2011), but the behaviour is similar.

The mean temperature profile for the second mode fundamental resonance and oblique breakdown case are shown in figure 34. They are compared with the modified Crocco–Busemann of Walz (1969), which includes the recovery factor in the quadratic velocity term for increased accuracy:

$$\frac{\tilde{T}}{T_e} = \frac{\tilde{T}_w}{T_e} + \frac{\tilde{T}_r - \tilde{T}_w}{T_e}\left(\frac{\tilde{u}}{u_e}\right) - r\frac{\gamma - 1}{2}M_e^2\left(\frac{\tilde{u}}{u_e}\right)^2. \qquad (3.19)$$

The current DNS results match well with Walz's equation especially in the turbulent region for both the first mode oblique breakdown and second mode fundamental resonance cases. There are slightly larger differences between the DNS results and Walz's equation in the transitional region, but the general shape still matches well.

The turbulent velocity fluctuations are another measure of a turbulent boundary layer. Figure 35 shows the streamwise, wall-normal, and spanwise velocity fluctuations for the first mode oblique breakdown case for two different x-locations. The u'_{rms}, v'_{rms} and w'_{rms} values are density-weighted according to Morkovin's scaling. The results (lines) here are compared qualitatively with temporal DNS results (square symbols) of Duan *et al.* (2011) for a Mach 5.8 boundary layer with $Re_\theta = 5775.1$ using y/δ_{99} scaling. In the transitional region ($x = 650$), the streamwise fluctuations are significantly higher than in the fully turbulent region ($x = 950$). The spanwise and wall-normal peak velocity fluctuations are similar in the transitional and fully turbulent regions, but have slightly different shapes. Comparing with the results of Duan *et al.* (2011),
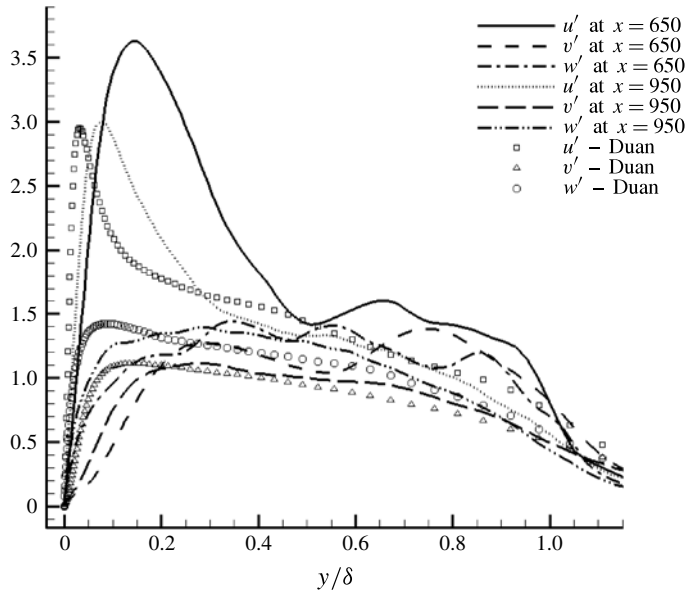
FIGURE 35. Wall scaled turbulent fluctuations at different *x* locations for the first mode oblique breakdown case compared with Duan *et al.* (2011).

the streamwise fluctuations in the turbulent region have the same peak magnitude and similar shapes. The peaks for all three velocity components do not match in location if scaled by boundary layer thickness because the Reynolds numbers are different. However, the results do compare well qualitatively. The maximum turbulent fluctuations for the streamwise and spanwise velocity components were previously shown in figure 21 for all three cases. The turbulent fluctuations as a function of wall distance are not shown here for the second mode fundamental resonance and three-dimensional cases but can be found in Franko (2011). In all three forcing cases, the streamwise velocity fluctuations are larger in the transitional region than in the turbulent region.

As the flow transitions from laminar to transitional to turbulent flow, energy moves from large scales to smaller scales. Development of the turbulent spectrum can easily be extracted in the spanwise direction because of its homogeneity. Figure 36 shows the development of the spectrum for the quantities $u'u'$, $v'v'$ and $w'w'$: see (3.10). The first figure shows the spectrum in the early transitional region for the oblique case at a wall-normal location of $y^+ = 25$. Clear peaks can be seen in the spectrum which correspond to harmonics of the oblique waves forced through suction and blowing. As the flow progresses further downstream, these peaks decrease and the expected spectrum for a fully turbulent flow is obtained. The inertial subrange can clearly be seen as it matches with the $\beta^{-5/3}$ law. The dissipation range can also be seen. The flow is nearly developed by the end of the domain, with little evidence of the initial forcing that leads to transition to turbulence.

For the second mode fundamental resonance case, the spectrum follows a similar pattern except that the initial spectrum is not as noisy. This is because the initially forced dominant disturbance is two-dimensional. There are additional modes excited as noted in table 3, but at low magnitudes. As the flow develops in the streamwise direction, the spectrum becomes closer to that of a fully turbulent flow but does not
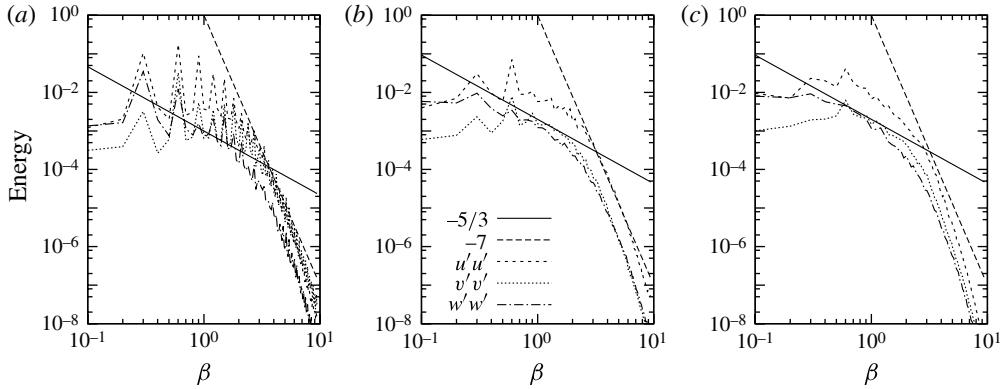
FIGURE 36. Spanwise energy spectrum of disturbances at different streamwise locations for $y^+ = 25$ for the first mode oblique breakdown case: (*a*) $x = 650$; (*b*) $x = 800$; (*c*) $x = 950$.
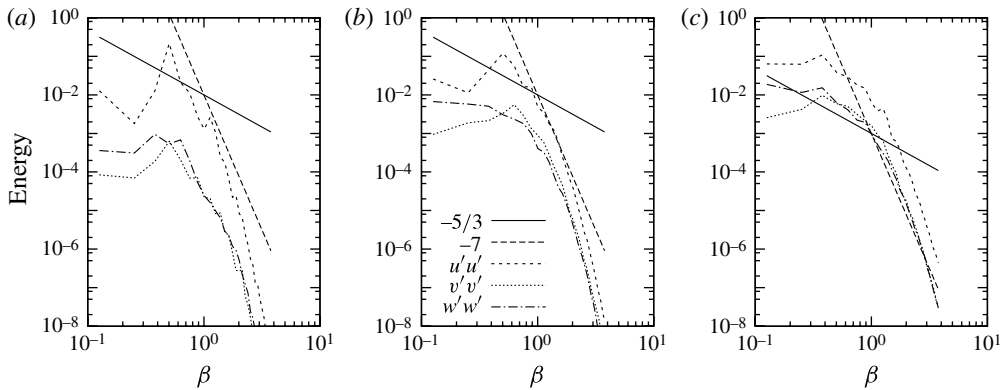

FIGURE 37. Spanwise energy spectrum of disturbances at different streamwise locations for $y^+ = 25$ for the second mode fundamental resonance case: (*a*) $x = 1000$; (*b*) $x = 1200$; (*c*) $x = 1400$.

clearly reach a fully turbulent state as in the first mode oblique breakdown case. This, in addition to the skin friction profile and mean streamwise velocity profiles, shows that the flow is still developing into a fully turbulent flow at the end of the domain.

For the second mode oblique breakdown case, the spectrum (see figure 38) also contains the harmonics of the initial disturbance as in the first mode oblique breakdown case. The peaks of this disturbance decrease as the flow develops in the streamwise direction, in a similar way to the first mode oblique breakdown case. By the end of the domain ($x/\delta_{in}^* = 1750$), the spectrum begins to take the form of a fully turbulent boundary layer flow.

4. Conclusions

Three different types of initial forcing were used in order to produce a transitional hypersonic boundary layer. For the first mode oblique breakdown case, the boundary layer transitions to a turbulent state. Also, in this case, both skin friction and
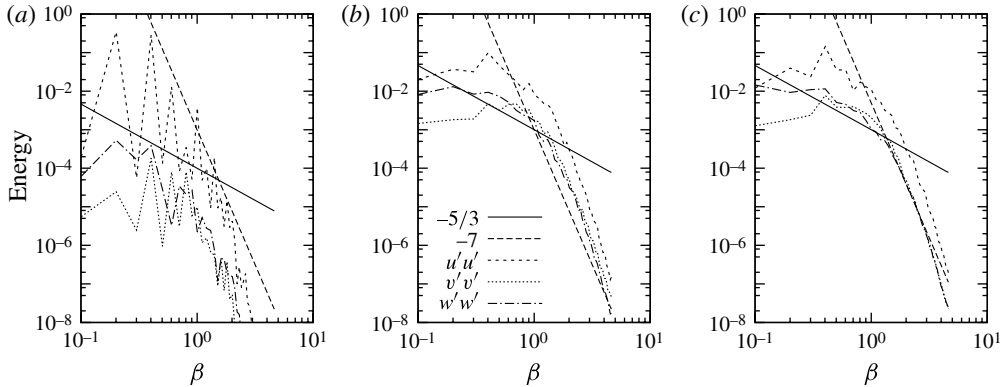
FIGURE 38. Spanwise energy spectrum of disturbances at different streamwise locations for $y^+ = 25$ for the second mode oblique breakdown case: (*a*) $x = 1200$; (*b*) $x = 1600$; (*c*) $x = 1750$.

heat transfer overshoots beyond turbulent correlation values are observed in the transitional region. For the second mode fundamental resonance and second mode oblique breakdown forcing cases, the boundary layers do begin to transition further downstream, but a fully turbulent flow is not obtained before the end of the domain. Transitional regions are long in these latter cases and the initial forced disturbances do not directly lead to transition. Overshoot of skin friction or heat transfer is not observed in the second mode fundamental resonance forcing case, but a slight heat transfer overshoot is observed in the second mode oblique breakdown case.

For the first mode oblique breakdown case, the overshoot in heat transfer and skin friction is caused by the interaction of the oblique modes, which leads to the generation of strong streamwise vorticity and the rapid breakdown of the boundary layer. This vorticity leads to the generation of high- and low-momentum streaks in the boundary layer and to large regions of high wall heat transfer in the transitional region. Evidence of this additional transport in the wall-normal direction of both streamwise momentum and thermal energy can be seen in the plots of Reynolds shear stresses and heat fluxes. The streaks generated have large amplitudes and quickly break down.

The first mode oblique breakdown case leads to fully turbulent boundary layers as shown by the scaled mean profile, the turbulent fluctuating quantities, and the spanwise spectrum. In contrast, the second mode fundamental resonance and second mode oblique breakdown forcing lead to later transition locations and boundary layers which are still developing to turbulence. While the second mode fundamental resonance and second mode oblique breakdown cases only explore one specific set of flow conditions and forcing parameters, the results match with previous computations (Pruett & Chang 1995; Koevary *et al.* 2010). For the second mode fundamental resonance case, the growth of the large two-dimensional wave leads to the generation of oblique modes with the same frequency. However, the secondary instabilities generated do not directly lead to breakdown, and breakdown occurs much further downstream as the generated streaks break down. In the second mode oblique breakdown case, the interaction of two oblique Mack modes does lead to the generation of streamwise vorticity and streaks, but the streaks and vorticity generated are weak and the boundary layer only transitions much further downstream.

In all three forcing scenarios, the generation of streamwise streaks precedes the final breakdown process.

It is still unclear which specific mechanism is responsible for transition to turbulence in the high-speed boundary layer experiments that have reported heat transfer overshoot, but the first mode oblique breakdown scenario offers a potential explanation for the overshoot of wall heat transfer observed. For the Mach numbers under investigation and for conventional wind tunnels, first mode instabilities may play a role in the transition process.

For the very specific flow conditions in this work, first mode oblique breakdown leads to the earliest transition location, which is probably due to the specific set of condition under study. More importantly, the transitional region is much shorter for first mode oblique breakdown because the primary disturbances do not saturate and large streamwise vorticity and streaks are generated which almost immediately break down to turbulence. In contrast, Mack second mode instabilities saturate once their amplitudes grow large. Forcing at a lower fundamental frequency could lead to a larger amplitude downstream based on linear theory, but saturation of the primary mode is still expected and the transition mechanism would remain the same. For two-dimensional Mack second mode instabilities, oblique disturbances are generated through fundamental resonance, which then generate streaks. These streaks are not as strong as for the pair of first mode oblique disturbances and therefore the streak instability grows more slowly and breakdown occurs later. The pair of second mode oblique waves also saturate and produce less vorticity and weaker streaks than the first mode oblique breakdown. Because second mode disturbances saturate without immediately producing turbulent flow, and first mode disturbances do not saturate and generate strong streaks that quickly break down, using the same N factor criterion for both first and second mode instabilities may not be appropriate. This is supported by experiments on a flared cone (Chou *et al.* 2011), where the N factors at the end of the cone are computed to be 14 but transition barely occurs at the end of the model. However, the streamwise streaks in wall heat transfer are observed earlier in the model after the maximum amplitude of the dominant second mode. Therefore, while using N factors may be useful in determining the saturation location of a second mode instability, breakdown may occur much further downstream.

Since the growth rates of disturbances will change depending on Mach number, Reynolds number and wall boundary conditions, it is difficult to conclude which mechanism will be dominant without taking all of these parameters into consideration. With increased wall cooling second mode instabilities will be dominant, and based on the simulations with increased wall cooling presented herein, the second mode fundamental resonance mechanism does not change with increased wall cooling. While linear growth is a starting point for transition prediction, it does not take into account the initial receptivity of instability waves or the nonlinear processes which eventually lead to breakdown. Receptivity, including the effects of isolated and discrete roughness, needs to be studied in detail to establish the initial amplitudes of instability modes excited. This is an area of active research. As shown in this work, it is also important to consider the nonlinear behaviour of the flow and the entire breakdown mechanism. Further exploration of different flow conditions is needed to determine which mechanisms are most important for high-speed boundary layer transition to turbulence under a range of parameters. However, first mode oblique breakdown is one likely mechanism of the heat transfer overshoot observed in experiments.

Acknowledgements

REFERENCES

ADAMS, N. A. & KLEISER, L. 1996 Subharmonic transition to turbulence in a flat plate boundary layer at Mach number 4.5. *J. Fluid Mech.* **317**, 301–335.

ALBA, C. R., CASPER, K. M., BERESH, S. J. & SCHNEIDER, S. P. 2010 Comparison of experimentally measured and computed second-mode disturbances in hypersonic boundary-layers. *AIAA Paper* 2010-897.

ANDERSSON, P., BRANDT, L., BOTTARO, A. & HENNINGSON, D. S. 2001 On the breakdown of boundary layer streaks. *J. Fluid Mech.* **428**, 29–60.

BEAM, R. M. & WARMING, R. F. 1978 An implicit factored scheme for compressible Navier–Stokes equations. *AIAA J.* **16**, 393–402.

BHASKARAN, R. 2010 Large eddy simulation of high pressure turbine cascade. PhD thesis, Stanford University, Stanford, CA.

BRADSHAW, P. 1977 Compressible turbulent shear layers. *Annu. Rev. Fluid Mech.* **9**, 33–54.

BRANDT, L. & HENNINGSON, D. S. 2002 Transition of streamwise streaks in zero-pressure-gradient boundary layers. *J. Fluid Mech.* **472**, 229–261.

CHOU, A., WARD, C. A. C., LETTERMAN, L. E., LUERSEN, R. P. K., BORG, M. P. & SCHNEIDER, S. P. 2011 Transition research with temperature-sensitive paints and in the Boeing/AFOSR Mach-6 quiet tunnel. *AIAA Paper* 2011-3872.

COLLIS, S. S. 1997 A computational investigation of receptivity in high-speed flow near a swept leading-edge. PhD thesis, Stanford University.

COOK, A. W. & CABOT, W. H. 2004 A high-wavenumber viscosity for high-resolution numerical methods. *J. Comput. Phys.* **195**, 594–601.

COOK, A. W. & CABOT, W. H. 2005 Hyperviscosity for shock–turbulence interactions. *J. Comput. Phys.* **203**, 379–385.

COSSU, C., BRANDT, L., BAGHERI, S. & HENNINGSON, D. S. 2011 Secondary threshold amplitudes for sinuous streak breakdown. *Phys. Fluids* **23**, 074103.

DHAWAN, S. & NARASIMHA, R. 1958 Some properties of boundary layer flow during transition from laminar to turbulent motion. *J. Fluid Mech.* **3**, 418–436.

DUAN, L., BEEKMAN, I. & MARTIN, M. P. 2010 Direct numerical simulation of hypersonic turbulent boundary layers with varying free stream Mach number. *AIAA Paper* 2010-353.

DUAN, L., BEEKMAN, I. & MARTIN, M. P. 2011 Direct numerical simulation of hypersonic turbulent boundary layers. Part 3. Effect of Mach number. *J. Fluid Mech.* **672**, 245–267.

FEDOROV, A. V. 2003 Receptivity of a high-speed boundary layer to acoustic disturbances. *J. Fluid Mech.* **491**, 101–129.

FEDOROV, A. V. 2011 Transition and stability of high-speed boundary layers. *Annu. Rev. Fluid Mech.* **43**, 79–95.

FERNHOLZ, H. H. & FINLEY, P. J. 1996 The incompressible zero pressure gradient boundary layer: an assessment of the data. *Prog. Aerosp. Sci.* **32**, 245–311.

FRANKO, K. 2011 Linear and nonlinear processes in hypersonic boundary layer transition to turbulence. PhD thesis, Stanford University.

FRANKO, K., BHASKARAN, R. & LELE, S. 2011 Direct numerical simulation of transition and heat-transfer overshoot in a Mach 6 flat plate boundary layer. *AIAA Paper* 2011-3874.

GUARINI, S. E., MOSER, R. D., SHARIFF, K. & WRAY, A. 2000 Direct numerical simulation of a supersonic turbulent boundary layer at Mach 2.5. *J. Fluid Mech.* **414**, 1–33.

HŒPFFNER, J., BRANDT, L. & HENNINGSON, D. S. 2005 Transient growth on boundary layer streaks. *J. Fluid Mech.* **537**, 91–100.

HOLDEN, M. S. 1972 An experimental investigation of turbulent boundary layers at high Mach number. NASA *Contractor Rep.* 111242.

HOPKINS, E. J. & INOUYE, M. 1971 An evaluation of theories for predicting turbulent skin friction and heat transfer on flat plates at supersonic and hypersonic Mach numbers. *AIAA J.* **9**, 993–1003.

HORVATH, T. J., BERRY, S. A. & HOLLIS, B. R. 2002 Boundary layer transition on slender cones in conventional and low disturbance Mach 6 wind tunnels. *AIAA Paper* 2002-2743.

HUSMEIER, F. & FASEL, H. 2007 Numerical investigations of hypersonic boundary layer transition for circular cones. *AIAA Paper* 2007-3843.

JIANG, L., CHOUDHARI, M., CHANG, C.-L. & LIU, C. 2006 Numerical simulations of laminar–turbulent transition in supersonic boundary layer. *AIAA Paper* 2006-3224.

JOHNSEN, E., LARSSON, J., BHAGATWALA, A. V., CABOT, W. H., MOIN, P., OLSON, B. J., RAWAT, P. S., SHANKAR, S. K., SJÖGREEN, B., YEE, H. C., ZHONG, X. & LELE, S. K. 2010 Assessment of high-resolution methods for numerical simulations of compressible turbulence with shock waves. *J. Comput. Phys.* **229**, 1213–1237.

KACHANOV, Y. S. 1994 Physical mechanisms of laminar-boundary-layer transition. *Annu. Rev. Fluid Mech.* **26**, 411–482.

KAWAI, S., SHANKAR, S. K. & LELE, S. K. 2010 Assessment of localized artificial diffusivity scheme for large-eddy simulation of compressible turbulent flows. *J. Comput. Phys.* **229**, 1739–1762.

KIMMEL, R. L. 1993 Experimental transition zone lengths in pressure gradient in hypersonic flow. In *Transitional and Turbulent Compressible Flows* (ed. L. D. Kral & T. A. Zang). ASME.

KLOKER, M. 2002 DNS of transitional boundary-layer flows at sub- and hypersonic speeds. In *DGLR Paper* JT2002-017, DGLR-Jahrestagung, Stuttgart, Sept. 2002.

KOEVARY, C., LAIBLE, A., MAYER, C. & FASEL, H. 2010 Numerical simulations of controlled transition for a sharp circular cone at Mach 8. *AIAA Paper* 2010-4598.

KRISHNAN, L. & SANDHAM, N. D. 2006 Effect of Mach number on the structure of turbulent spots. *J. Fluid Mech.* **566**, 225–234.

LELE, S. K. 1992 Compact finite-difference schemes with spectral-like resolution. *J. Comput. Phys.* **103**, 16–42.

MA, Y. & ZHONG, X. 2003*a* Receptivity of a supersonic boundary layer over a flat plate. Part 1. Wave structures and interaction. *J. Fluid Mech.* **488**, 31–78.

MA, Y. & ZHONG, X. 2003*b* Receptivity of a supersonic boundary layer over a flat plate. Part 2. Receptivity to free stream sound. *J. Fluid Mech.* **488**, 79–121.

MA, Y. & ZHONG, X. 2005 Receptivity of a supersonic boundary layer over a flat plate. Part 3. Effects of different types of free stream disturbances. *J. Fluid Mech.* **532**, 63–109.

MACK, L. M. 1969 Boundary layer stability theory. Jet Propulsion Laboratory document 900-277 (Rev A).

MALIK, M. R., SPALL, R. E. & CHANG, C. L. 1990 Effects of nose bluntness on boundary layer stability and transition. *AIAA Paper* 1990-0112.

MARTIN, M. P. 2007 Direct numerical simulation of hypersonic turbulent boundary layers. Part 1. Initialization and comparison with experiments. *J. Fluid Mech.* **570**, 347–364.

MASAD, J. A. 1993 Relationship between transition and modes of instability in supersonic boundary layers. NASA *Contractor Rep.* 4562.

MASLOV, A. A., SHIPLYUK, A. N., SIDORENKO, A. A. & ARNAL, D. 2001 Leading-edge receptivity of a hypersonic boundary layer on a flat plate. *J. Fluid Mech.* **426**, 73–94.

MAYER, C. S. J., VON TERZI, D. A. & FASEL, H. F. 2011 Direct numerical simulation of complete transition to turbulence via oblique breakdown at Mach 3. *J. Fluid Mech.* **674**, 5–42.

NAGARAJAN, S. 2004 Leading edge effects in bypass transition. PhD thesis, Stanford University.

NAGARAJAN, S., LELE, S. K. & FERZIGER, J. H. 2003 A robust high-order compact method for large eddy simulation. *J. Comput. Phys.* **191**, 392–419.

NARASIMHA, R. 1985 The laminar–turbulent transition zone in the boundary layer. *Prog. Aerosp. Sci.* **22**, 29–80.

PIROZZOLI, S., GRASSO, F. & GATSKI, T. B. 2004 Direct numerical simulation and analysis of a spatially evolving supersonic turbulent boundary layer at $M = 2.25$. *Phys. Fluids* **16**, 530–545.

PRUETT, C. D. & CHANG, C.-L. 1995 Spatial direct numerical simulation of high-speed boundary layer flows. Part 2. Transition on a cone in Mach 8 flow. *Theor. Comput. Fluid Dyn.* **7**, 397–424.

ROY, C. J. & BLOTTNER, F. G. 2006 Review and assessment of turbulence models for hypersonic flows: 2D/axisymmetric cases. *AIAA Paper* 2006-713.

SCHLATTER, P., BRANDT, L., DE LANGE, H. C. & HENNINGSON, D. S. 2008 On streak breakdown in bypass transition. *Phys. Fluids* **20**, 101505.

SCHNEIDER, S. P. 2001 Effects of high-speed tunnel noise on laminar–turbulent transition. *J. Spacecr. Rockets* **38**, 323–333.

SIVASUBRAMANIAN, J. & FASEL, H. F. 2010 Numerical investigation of boundary layer transition initiated by a wave packet for a cone at Mach 6. *AIAA Paper* 2010-900.

STETSON, K. F. & KIMMEL, R. L. 1992 On hypersonic boundary-layer stability. *AIAA Paper* 1992-0737.

STETSON, K. F. & KIMMEL, R. L. 1993 On the breakdown of a hypersonic laminar boundary layer. *AIAA Paper* 1993-0896.

THUMM, A., WOLZ, W. & FASEL, H. 1990 Numerical simulation of spatially growing three-dimensional disturbance waves in compressible boundary layers. In *IUTAM Symposium on Laminar–Turbulent Transition* (ed. D. Arnal & R. Michel), pp. 303–308. Springer.

WADHAMS, T. P., MUNDY, E., MACLEAN, M. G. & HOLDEN, M. S. 2008 Ground test studies of the HIFiRE-1 transition experiment part 1: experimental results. *J. Spacecr. Rockets* **45**, 1134–1148.

WALZ, A. 1969 *Boundary Layers of Flow and Temperature*. MIT.

WANG, M., LELE, S. K. & MOIN, P. 1996 Sound radiation during local laminar breakdown in a low-Mach-number boundary layer. *J. Fluid Mech.* **319**, 197–218.

WHITE, F. M. 2006 *Viscous Fluid Flow*. McGraw-Hill.

WILKINSON, S. P. 1997 A review of hypersonic boundary layer stability experiments in a quiet Mach 6 wind tunnel. *AIAA Paper* 1997-1819.

XIONG, Z. & LELE, S. K. 2004 Distortion of upstream disturbances in a Hiemenz boundary layer. *J. Fluid Mech.* **519**, 201–232.